Rhodanine composite fluorescence probes to detect amyloid-beta aggregated species in Alzheimer's disease models

Himanshu Rai
Indian Institute of Technology (Banaras Hindu University) https://orcid.org/0000-0002-5615-5058
Rishabh Singh
All India Institute of Medical Sciences
Prahalad Bharti
All India Institute of Medical Sciences
Prabhat Kumar
Institute of Science, Banaras Hindu University
Sanskriti Rai
All India Institute of Medical Sciences
Tanmay Varma
National Institute of Pharmaceutical Education and Research (NIPER),
Brijesh Singh Chauhan
Institute of Science, Banaras Hindu University
Aishwarya Nilakhe
National Institute of Immunology
Joy Debnath
SASTRA Deemed University
Vijay Mishra
Institute of Medical Sciences, Banaras Hindu University
Sarika Gupta
National Institute of Immunology
Sairam Krishnamurthy
Indian Institute of Technology (Banaras Hindu University)
Jian Yang
School of Medicine, Shanghai University
Prabha Garg
National Institute of Pharmaceutical Education and Research (NIPER)
Saripella Srikrishna
Institute of Science, Banaras Hindu University
Saroj Kumar

All India Institute of Medical Sciences

Gyan Modi (gpmodi.phe@itbhu.ac.in)

Indian Institute of Technology (Banaras Hindu University) https://orcid.org/0000-0002-8003-5566

Article

Keywords: Alzheimer's disease, β-amyloid (Aβ) aggregates, bovine serum albumin (BSA), carbostyril, coumarin, rhodanine dyes, near-infrared (NIR) probes

Posted Date: April 5th, 2023

DOI: https://doi.org/10.21203/rs.3.rs-2721179/v1

Abstract

Molecular near-infrared (NIR) imaging is an emerging pre-clinical tool for labeling Alzheimer's disease (AD) pathogenic biomarkers, especially cerebral amyloid-beta (Aβ) plaques. Herein, we present a series of acceptor-π-donor based molecular NIR probes, composed of rhodanine (acceptor fragment) in conjugation with coumarin or carbostyril (donor fragment) nucleus. The most promising probe **19** has a desirable binding affinity (K_d = 0.143 μM) against Aβ aggregates with little or no nonspecific interaction with BSA, minimal cytotoxicity, good brain permeability, desirable plasma stability, and fluorescence sustainability profile across a comprehensive physiological pH range. Histological fluorescence imaging revealed that probe **19** had good selectivity and affinity for Aβ plaques, confirmed with immunofluorescence and ThT (aggregated Aβ specific dye), and a high signal-to-noise ratio. It was also successfully applied for fluorescence labeling of Aβ in the eye imaginal disc of AD Drosophila larvae. Collectively, these probes can be finetuned due to their versatile structural scaffold to evolve as promising NIR imaging probes for the detection of AD biomarkers.

1. Introduction

Alzheimer's disease (AD) is a devastating brain-related disorder onset as deficits in episodic memory that worsen with aging.(1) While the cognitive deficit is the cardinal feature of AD, the onset of AD neurodegeneration begins as a long asymptomatic preclinical phase (20–30 years), where the cognitive deficit is unnoticeable to the person suspected of AD. The failure of prescribed medications to cure AD is due to a multifaceted etiology and the use of therapeutics at an advanced stage when significant irreversible brain atrophy has already occurred. As a result, early AD diagnosis is crucial to ensure timely and effective treatment before irreversible neuronal atrophy becomes widespread.

Early-stage factors underlying brain atrophy in AD etiology are still elusive. However, several factors, including age, gender(2), deposition of misfolded amyloid-beta (Aβ) peptides, Tauopathies, genetic manipulation(3), depletion of cholinergic neurons(4, 5), elevated reactive oxygen species (ROS) levels(6–8), and bio-metal ions (Cu^{2+}, Fe^{2+}, and Zn^{2+}) dyshomeostasis, etc. are tightly intertwined mechanistically in AD etiology.(9, 10) Advancement in neurobiology revealed a close relationship between depth of severity in terms of cognitive decline and progressive neuronal atrophy with the elevated level of aggregated toxic Aβ species and filamentous neurofibrillary tangles (NFTs).(11, 12) Several studies have corroborated that these biomarkers begin to produce long before clinical symptoms manifest in an AD suspect. Consequently, the misfolded Aβ species and NFTs are gained more attention and have become the most extensively used biomarkers for early AD diagnosis. Therefore, *in-vivo* detection of these biomarkers has significant relevance as the predictive indicators for the definitive differential diagnosis from other brain anomalies. Additionally, these AD prognostic biomarkers may offer realistic opportunities to facilitate studies in determining the potential of novel disease-modifying or preventive therapies in AD.

In its preclinical or clinical phase, a differential AD diagnosis requires extensive behavioral studies and radiolabeled neuroimaging techniques such as PET imaging, which is a relatively costly and time-consuming process. For a definitive diagnosis, histopathological brain tissue staining for marker proteins of AD can only be done after the patients died. Thus, a high-performance, *in-vivo* imaging tool which could acquire real-time data using readily available, cheap, and easy operational machinery can become a viable option. The existing *in-vivo* imaging modalities, especially PET diagnosis, are very expensive and not readily available for primary patient screening or in preclinical investigations. Other disadvantages including unavoidable radiation exposure from the radio-labeled substrate, limited isotope availability, short isotope shelf life, and lengthy data processing hinder the extensive application. Whereas visible (emission wavelength below 600 nm) fluorescent imaging is not applicable for *in-vivo* detection due to the maximal photon scattering occurs before reaching the camera for image capturing and the limited depth of tissue penetration.(13) On the other hand, light in the far red or near-infrared (600–900 nm) region could penetrate deeper into deeper tissue due to its low absorption coefficient property and negligible quenching from nonspecific tissue autofluorescence, resulting in a higher target-to-background ratio.(14) Thus, molecular probes with long emission wavelengths in the deep red or near-infrared region are thought to be the best for *in-vivo* imaging. Moreover, rationally designed molecular NIR probes can be modified by substituting appropriate radioisotopes for multimodality imaging by merging nuclear imaging with optical imaging, which could complement current imaging methods. Additionally, using advanced techniques like fluorescence molecular tomography (FMT), hyperspectral imaging, and ocular imaging methodologies in integration with NIRF imaging can be translated into clinically useful *in-vivo* imaging signals in the near future.(15, 16) Therefore, the last two decades witnessed an exponential growth of fluorescent molecular probe application in neuroimaging due to high performance in preclinical studies.(17) Even though some NIR probes have shown promising results, there are still several challenges to overcome for NIR probes to be employed successfully in monitoring AD pathogenesis. Thioflavin T (ThT), Thioflavin-S (ThS), and Congo Red (CR) are conventional dyes with limited applicability, i.e., restricted to histopathological staining of senile plaques. Likewise, FDA approved the use of three ^{18}F-labeled radioisotopes ($T_{1/2}$ = 109.7 min) [^{18}F-AV-45 (florbetapir), BAY94-9172 (florbetaben), and ^{18}F-flutemetamol] and ^{11}C-labeled radioisotopes ($T_{1/2}$ = 20.4 min) Pittsburgh compound-B [^{11}C-(PIB)] as Positron emission tomography (PET) contrast agent for definite diagnosis of AD.(18) Previously, NIR probes from several versatile scaffolds, such as BODIPY-based fluorescent probes (BAP-1/2 for Aβ plaques(19) and BD-Oligo for Aβ oligomers(20)), CRANAD-derived probes (CRANAD-2 for insoluble Aβs, CRANAD-65 for selective oligomeric Aβs and CRANAD-58 for all forms of Aβs)(21) and DANIR probes (DANIR 3b and DANIR 8c)(22) have been successfully applied for detecting Aβ plaques in small animal models with *in-vivo* NIR imaging efficacy.

In this work, we utilized the conventional donor-π-acceptor (D-π-A) structural motif to develop novel *in-vivo* biosensing NIR probes for detecting potential pathogenic indicators of AD. The designed probes consist of *N, N*-dimethylamine substituted (C-7 position) coumarin, and carbostyril as a key core nucleus integrated with electron-deficient rhodanine-based acceptor fragments as shown in Fig. 1. Typically, coumarin has the maximum absorption and emission wavelengths in a relatively shorter wavelength

region with poor fluorescence quantum yield (Φ_F, Fig. 1). However, the substitution with appropriate electron donor and acceptor moiety in *vide infra* structural framework (D-π-A fashion) induces intramolecular charge transfer (ICT), resulting in improved photophysical properties, such as increasing the QY (Φ_F) value and extending the fluorescence emission maxima.(23) We believe that coumarin (2H-chromen-2-one) and carbostyril (2-quinolone) core nuclei with extended π-electron polyene elongation and planer geometry, can facilitate electronic delocalization, which could result in a much narrower bandgap between HOMO–LUMO states shift emission wavelength towards deep-red or NIR spectral range (650–900 nm), an ideal range for *in-vivo* bioimaging. To the best of our knowledge, this is the first time to compare the NIR potential of a 2-quinolone core to that of 2H-chromen-2-one in AD.

2. Results And Discussion

For an ideal NIR fluoroprobe to meet the diverse, multifaceted, and complex neurobiology of the AD brain, the following are the qualifying requirements: (a) photophysical properties like emission wavelength of NIR spectral range (650–900 nm), large Stokes shift with high fluorescence quantum yield (QY), change in fluorescent properties on interactions with target biomarkers, high signal to noise (S/N) ratio, and high selectivity, (b) biochemical properties like efficient BBB permeability, strong binding affinity, minimal nonspecific interaction from the surrounding biologics, low toxicity, and (c) planar rigid molecule with small molecular size (mass less than 600) with good lipophilicity (log p-value between 1 and 3).(24) Moreover, for a viable NIR probe, it should be compatible and stable within the biological system.(25)

2.1. Rational behind the design of novel NIR probes:

Previous studies revealed that *N, N*-dimethylamino group is an ideal electron rich-donor and played an important role in recognizing *β*-sheet structure(*25–27*), which could promote substituent Aβ binding affinity. Also, the planar geometry of the *N, N*-dimethylamino group can facilitate efficient electron delocalization *via* ICT in extended conjugation within the core nucleus system. Several NIR probes, such as BCB-1,(28) IRI-1,(29) and CQ,(30) (Fig. 1), showed the coumarin scaffold had the capability to identify amyloid fibrils efficiently with excellent selectivity. In recently study, fluoroprobes based on phenothiazine-rhodanine were found to be efficient for *in-vivo* fluorescence imaging of amyloid-β plaques and inhibition of Aβ aggregation in animal models.(26) These experimental data thus suggested, in a different context, that rhodanine could be developed into a potential candidate against AD with Aβ modulatory activity. Recently, Elbatrawy, A. A., et al. (2021) developed a quinoline-based “Turn-On” fluorescent probe (Q-tau 4) (31) that exhibited emission maxima in the red region (630 nm) and nanomolar binding affinity (K_d = 16.6 nM) to tau aggregates. Similarly, quinoxaline ring successfully applied in NIR probes such as tau tangles specific dye QNN-3b(32) and Aβ aggregates specific dye QN-18(33) has a potential core with hetero-atom (N) infers that methodical design engineering can result in adaptable NIRF probes with appropriate optical properties and metabolic stability. Therefore, we developed probes by replacing the oxygen atom with NH in coumarin-based dyes to monitor the impact on optical and biological affinity against the target species. Up to now, carbostyril-derived probes have not been explored in AD investigational studies yet.

Based on the following facts, we developed a series of NIRF imaging probes using the donor-π-acceptor structural motif (push-pull architecture), presuming that optimal optical properties along with a potential to satisfy the necessary requirements for cerebral Aβ species imaging that can be achieved with the aid of rational design strategy. Thus, the designed scaffold is composed of a coumarin or carbostyril donor fragment as an Aβ recognition moiety, and a rhodanine fragment with a variable carbon spacer to probe the role of linker length on optimising the optical and physiochemical properties of probes as well as interaction with Aβ aggregates. Herein, we report the synthesis, characteristics, and biological evaluations of these NIRF imaging probes for Aβ plaques in the AD *in-vitro* and *in-vivo* studies in the AD models.

2.2. Synthetic schemes and chemistry for the synthesis of rhodanine-based NIR probes (18–27; scheme 1–4)

The synthesis of the designed probes, as depicted in Scheme 1–4, is as follows: Scheme 1 describes the synthesis of key intermediate 7-(dimethylamino)-2-oxo-2H-chromene-3-carbaldehyde (5). Compound **2** was synthesized by using $POCl_3$/DMF as the formylating agent using the Vilsmeier-Haack reaction condition. Knoevenagel condensation was performed to develop coumarin scaffold **3** using diethyl malonate, which undergoes acid-mediated ester hydrolysis followed by decarboxylation to produce compound **4**. Finally, formylation at the 3-position was achieved using the Vilsmeier-Haack reaction condition to obtain intermediate **5**.

Synthesis of 3-formylcarbostyril analog (10): The acetylation of compound **6** produces *N*-Acetyl-3-floroaniline (7). Compound **7** was treated with $POCl_3$/DMF at 0° C and continued the stirring up to 70°C continuously for 8h to obtain compound **8** with 55% yield. Treatment of compound **8** with acetic acid at 100°C yielded compound **9.** Finally, the key intermediate **10** was achieved by treating **9** with *N*, *N*-dimethylamine hydrochloride salt in presence of K_2CO_3 (Scheme 2).

Scheme 3 outlined the synthetic approach for synthesizing rhodanine derivatives (**13-17**). Amino acids (generalized structures **11a-e**) were dissolved in KOH solution to generate a free amino group and ionization followed by sequential dropwise addition of CS_2 and chloroacetic acid. The final cyclization step was achieved by the use of con. H_2SO_4 to yield intermediates **13-17** with quantitative yield (40-65%).

Finally, the designed probes (**18–27**, scheme 4**)** were obtained by the condensation reaction of various substituted rhodanine-based acceptor analogs (13–17) at their activated methylene group with coumarin (inter. **5**) and carbostyril (inter. **10**) aldehydes in the presence of piperidine (cat.) as a base at 110°C. All the newly synthesized probes were purified by column chromatographic techniques and structurally characterized by ^{1}H-NMR and high-resolution mass spectrometry (HRMS, Table S1). Their spectral data are provided in the Supplementary data file (Fig. S1-S32, ESI†).

2.3. Spectroscopic properties of the synthesized probes:

The UV-visible and fluorescence data, including the excitation and emission wavelengths of these probes in DMSO and PBS (pH 7.4), are summarized in Table 1 and Figs. S33-S37 (ESI†). All the tested probes

were found to lie in red to near-infrared (NIR) emissions ranging from 610–660 nm in PBS and large Stokes shift (≥ 70 nm in DMSO and ≥ 120 nm in PBS), endowing them an *in-vivo* imaging ability and lower background interference (Table 1). To get more information about the TICT (Twisted Intramolecular Charge Transfer) progress in a D-π-A system and environmental viscosity, we systematically increase solvent viscosity by admixing glycerin to MeOH fractions in different ratios (0-100%: v/v) of probe **19** (1 μM) and then recorded the emission spectra at 510 nm. As shown in Fig. S38 (A), the fluorescence intensity increased steadily with the percentage of glycerol increased, with a correlation coefficient [R^2 = 0.925; Fig. S38 (B), ESI†], and tends to saturate at 80% glycerol fraction in MeOH. This experiment verifies the evident impact of glycerol viscosity on the fluorescence intensity of probe **19**. The probable reason behind this is that a viscous glycerol environment could prohibit the intramolecular rotation of **19** around the conjugated diene bridge leading to enhanced fluorescence intensity by the PICT (Photo Induced Intramolecular Charge Transfer) process. This result suggested that probe **19** may exhibit "Turn On" fluorescence phenomena in a viscous protein environment. Similarly, **19** also showed impressive solvatochromic shifts with increasing polarity of solvents [Fig. S39 (A-C), ESI†]. In particular, a bathochromic shift and enhancement of florescence intensity were observed when moving from toluene (low polarity) to DMSO (high polarity) in a linear fashion, with gradual change (enhance) in the color intensity under the ultraviolet (369 nm) illumination [Fig. S39 (A-C), ESI†], confers the probe sensitivity could employ to asses pathogenic changes in the biological microenvironment.

Table 1

The physicochemical and photochemical properties of the synthesized fluorescence dyes.

Sr. No.	Probe Id	Photophysical characteristics							cLog P¶
DMSO				λ (max, Em)‡ nm	λ (max, Em) § nm	Quantum yield (Φ_f) ||			
λ (max, Ab) nm	λ (max, Em)* nm	Stoke Shift (nm)	(⍰)† $M^{-1}cm^{-1}$						
1.	18	515	595	80	2.535×10^4	640	640	0.0697	2.32
2.	**19**	517	605	88	1.884×10^4	630	635	0.1337	2.62
3.	**20**	520	590	70	2.164×10^4	650	630	n.d.	2.87
4.	**21**	517	600	83	2.853×10^4	640	630	n.d.	3.30
5.	**22**	520	590	70	3.110×10^4	660	620	0.1457	3.67
6.	**23**	520	585	65	3.590×10^4	650	650	0.1808	2.37
7.	**24**	515	594	79	2.064×10^4	650	660	n.d.	2.47
8.	**25**	495	575	80	2.664×10^4	610	610	n.d.	2.75
9.	**26**	515	590	75	2.906×10^4	650	640	n.d.	3.09
10.	**27**	495	575	80	2.846×10^4	620	620	n.d.	3.45

*****Emission maxima measured in DMSO, †Molar absorptivity coefficient value determined in DMSO using equation Y = ε*X + C. ‡Emission maxima measured in PBS, §Emission maxima when bound to the A$\beta_{1\text{-}42}$ aggregates in PBS (pH 7.4). ||Relative quantum yield determined in DMSO using Rhodamine-B (Φ_f = 0.44 in DMSO) as reference standard, n.d. = not determined, ¶Calculated LogP values using ALOGPS 2.1 program.

Except for probes **21, 22**, and **27**, the calculated Log P values of the developed probes were found to be within the desirable range of 2.32–3.09 (Table S2, ESI†). Likewise, all probes have a molecular mass of

450 Dalton (Table S1, ESI†).

2.4. Fluorescence study of tested probes against various Aβ species, BSA, and Tau aggregates:

Literature evidence revealed that Aβ-mediated neurotoxicity is associated with peptide length (isoforms of Aβ peptide, especially $Aβ_{40,}$ and $Aβ_{42}$)(34) and their oligomerization states.(35) The $Aβ_{42}$ peptides were prone to aggregate and generate oligomeric species (principle toxin) following plaque formation.(36) Therefore, preliminary screening of developed probes was performed for their ability to detect $Aβ_{1-42}$ aggregates. Serum albumin is the most abundant plasma protein; therefore, it is crucial to determine the affinity of designed probes toward these proteins. It is preferential for a NIR Aβ-specific probes to have very little or no interactions with serum albumin. Thus, *In-vitro* fluorescence assay was performed to compare the fluorescent properties of probes (50 μM) in an aqueous solution (PBS, pH 7.4) to their fluorescence intensities in the presence of $Aβ_{1-42}$ aggregates (25 μM of $Aβ_{1-42}$ incubated for 72h in PBS 7.4 pH) and bovine serum albumin (BSA; 50 μg/mL). As shown in Fig. 2, there was no significant change in fluorescence upon incubation with BSA, suggesting that the test probes had little or no interaction with BSA. The coumarin-based probes, i.e., **19** and **22**, exhibited an increase in the fluorescence intensities against $Aβ_{1-42}$ aggregates (25 μM) with maxima at 635 and 629 nm, respectively (Table 1), whereas **18** displayed affinities for both $Aβ_{1-42}$ monomers and $Aβ_{1-42}$ aggregates with maxima at 640 nm. This data indicates that probe **19**, and **22** have higher affinities for aggregated Aβs. Carbostyril-based probes, i.e., **23**, also were found to exhibit enhanced fluorescence intensities after binding to both $Aβ_{1-42}$ monomers and $Aβ_{1-42}$ aggregates with emission maxima at 635 nm, whereas as rest of the probes displayed no marked affinities to Aβs (Fig. S41-a, ESI†). Additionally, the emission maxima falling in the red region (635 nm, very close to the NIR-1 range) of fluorescence spectra on interaction with $Aβ_{1-42}$ aggregates indicate that probes **18**, **19**, and **23** could have a propensity for in-vivo imaging. The variables at the core nucleus and length of rhodanine carbon spacers might play some contribution towards the affinities for aggregated species.

Coumarin-based probes, i.e., **19** and **22**, were also tested for their affinity towards various full-length tau aggregates. The study (Fig. S41-b, ESI†) revealed that both the probes (20 μM) responded to Tau aggregates (10 μM) with ~ 2-fold enhanced fluorescence intensity accompanied by a hypsochromic shift in the emission maxima of 30–50 nm. The data from Fig. 3 showed that the weak fluorescence of probes **19** and **22** in PBS (solid, red) and HEPES buffer (dotted, yellow) was intensified upon mixing with both amyloid (solid line, blue) and Tau aggregates (dotted line, green). Probe **19** displayed a 2.29-fold increase in intensity with Aβ aggregates, which is relatively higher compared to Tau aggregates (1.72-fold), suggesting that probe **19** has a better turn-on ability for Aβ aggregates. Additionally, the blue shift in emission maxima (605 nm) on interaction with tau aggregates, contrary to Aβ aggregates (635 nm), limits the *in-vivo* detection efficacy of probe **19** against tau species. Likewise, probe **22** displayed a similar trend, with 2.12- and 2.31-fold increases in fluorescence intensity with emission peaks for tau and

Aβ aggregates at 595 and 620 nm, respectively. Such distinct fluorescence behavior can be applied to detect pathogenic tau aggregates in *in-vitro* and *ex-vivo* labeling studies efficiently.

Based on the above finding, probes (**19** and **22)** with relatively higher selectivity for $A\beta_{1\text{-}42}$ aggregates and probe (18) with the most intensified signals against Aβs have been selected for further biological screening.

2.5. *In-vitro* Aβ aggregates binding constant assay of the developed probes:

Based on the fluorescent intensity enhancement in the presence of the aggregated $A\beta_{1\text{-}42}$ species, the binding affinities (K_d) of the probe **19** and **22** were quantitatively determined by a fluorescence-based saturation binding assay. The saturation binding curves in Fig. 4 demonstrated that probes **19** and **22** have binding affinities in the sub-μM range upon binding with $A\beta_{1\text{-}42}$ aggregates, which is higher than the traditional Aβ-specific dye Thioflavin-T (ThT; 890 ± 92 nM) (37). However, altered lipophilicity caused by the rhodanine carbon chain has a minor influence on fluorescence characteristics but appears to have a substantial impact on the binding affinities of the probes for the target protein.

2.6. pH-dependent stability testing of the promising probes (18, 19, and 22):

In addition, the fluorescence emission spectra of selective coumarin-based probes, i.e., **18**, **19**, and **22** (50 μM), were determined at various pH buffers (pH = 6, 6.7, 7.0, and 7.4) to mimic the physiological conditions. Three-way correlation graphs (Fig. S42, ESI†) showed that the fluorescence signal of the probes enhances exponentially as the pH value increased. Moreover, all the probes were stable at various biological pH upon incubation for 24 h (Fig. 5), except for **22**. As seen in Fig. 5C, the probe with a 5-carbon spacer at the rhodanine fragment (22) showed a substantial rise in fluorescence intensity with a slight increase in pH value. The most plausible explanation is that ionization increased with the basicity of the vehicle, which in turn increased the probe's solubility. These data further confirmed the solvatochromic and pH-specific microenvironment sensitivity of the probes. The probes' remarkable fluorescence photostability at selected physiological pH prompted us to conduct subsequent biological investigations.

2.7. Determination of cell viability using MTT assay

Low cytotoxicity is one of the essential criteria before moving to the *in-vivo* biological application of the developed probe. The cytotoxicity test of **18**, **19**, and **22** were performed in PC-12 cells by MTT assay. No marked cytotoxicity was observed up to 20 μM concentration of all tested probes after incubated over 24 h (Fig. 6), indicating their safety profile for the *in-vivo* application.

2.8. Stability study in the ICR mice plasma

HPLC purity of probe **19** and **22** was found to be ≥ 95.0% as shown in Fig. S43-44, ESI†. The optimal plasma stability is essential for effective *in-vivo* efficacy; therefore, a plasma stability study of the leader

probe **19** was performed in ICR mice plasma at various time points (0, 10, and 30 mins). The HPLC analysis (Fig. S45, ESI†) indicates that the probe has acceptable plasma stability with ≥ 85.0% purity over 30 min and could be used for *in-vivo* bioimaging.

2.9. Cell internalization studies

The cell internalization assay of probes **18**, **19**, and **22** was performed in PC12 cells to evaluate the functionality of probes to work in a live system. Cells were then treated with different concentrations of these probes (1, 5, and 10 μM, Fig. S47, ESI†). The results showed concentration-dependent internalization in PC12 cells. The probes are recorded to have efficient cytoplasmic distribution in PC12 cells, rendering them suitable for bioimaging (Fig. 7). Also, Fig. S46 indicates that probes showed intracellular fluorescent signaling enhancement in a dose-dependent manner and maintained normal cellular activity without any sign of cell viability. It can be used for imaging morphological changes at a sub-microscopic level and has proven to be useful in studying cellular physiology at the biomolecular level.

2.10. *In-vitro* fluorescent staining of brain slice sectioned from *APP/PS1* mice

Next, to validate the specificity and sensitivity of the tested probes for amyloid beta plaques, neuropathological fluorescence staining was performed for leader probe **19** and **22** in the *APP-PS1* mice brain slices before moving to *in-vivo* imaging in live animal model. Both the probes were incubated with the brain slice of a 14-month-old *APP/PS1* mice for 30 mins. Fluorescence microscopy observations showed numerous Aβ plaques were lit up in the cortex and hippocampal region of brain on staining with probe **19** and **22**, as shown in the Fig. 8A&E respectively, and when costained with Thioflavin T (ThT), the signals were observed in the same region (Fig. 8B&F). Despite colocalized signals of probe **22** with ThT (Fig. 8G&H), additional staining pattern were observed that may associated with non-specific binding. This data suggests that probes **19** could specifically highlight Aβ plaques demonstrating excellent colocalization with ThT staining, the gold standard staining for Aβ plaques, as shown in the merged and scale up images (Fig.s 8C&D).

2.11 Assessment of BBB permeability and performance of probe 19 in in-vivo fluorescence imaging in APP/PS1 AD mouse model

Encouraged by the above findings, we further investigated the potential of probe **19** for BBB permeability and *in-vivo* detection efficiency. The 13-month-old *APP/PS1 (Tg)* and aged-matched normal *C57BL/6* wild-type (WT) mice were (n = 3) intravenously injected 100 μL of probe **19** (0.8 mg/kg; the vehicle used for dilution consisted of 15% of DMSO, 5% of Cremophor® EL, and 80% of 1X PBS) *via* the tail vein. The transgenic (*Tg*-AD) mice show an age-dependent increase in amyloid burden and develop accelerated plaque pathology with aging. Increased levels of Aβ are also visible in the brain of mice as early as 4–6 months of age.(38) Thus, these mice were chosen for NIR fluorescence imaging and captured their brain signals at various time points (5, 15, 30, 60, and 90 min) to assess in-vivo imaging efficacy. *In-vivo* brain

imaging data from Fig. 9A verify that the probe has efficient brain permeability. Additionally, the data indicate that fluorescence signals in the *Tg*-AD mice are relatively higher than in the age-matched littermates, which may be attributed to the binding of the probe to the Aβ aggregates, which prolonged its retention period. Images at different time points (Fig. 9A and B) indicated that intense brain fluorescence signals were observed in both the mice at 5 min after intravenous injection of probe **19**, which gradually starts decaying after 30 min, and almost all the signals were diminished at 90 min. The brain signals recorded at representative time points show that fluorescence signals are relatively higher in *Tg*-AD mice than in WT mice, as shown in Fig. 9B. According to these findings, we may infer that probe **19** has a good brain kinetic profile, including fast brain uptake and a quick washout rate, a highly desirable feature for *in-vivo* brain imaging.

Furthermore, to substantiate the *in-vivo* brain imaging, *ex vivo* experiments were performed. As shown in Fig. 10A compared to mice that received vehicle alone (Blank; ROI 1: 4.57e + 8), WT and *Tg*-AD mice have nearly equivalent brain fluorescence signals with 2.5-fold amplified intensity (ROI 2 and 3: 1.14 and 1.18e + 9, respectively). The *ex vivo* fluorescence observation of the excised and perfused brains from the mice sacrificed at 20 min post tail vein injection of probe **19** (0.8 mg/kg; 100 µL of the vehicle consisting of 15% of DMSO, 5% of Cremophor® EL, and 80% of 1X PBS) showed 1.45 fold higher fluorescence signal in the brain of *Tg*-AD mouse (ROI 3 = 1.25e + 9; Fig. 10B) compared to WT mice brain (ROI 2 = 8.63e + 8), which may attribute to the specific binding (response) of probe **19** for cerebral Aβ plaques. Additionally, vital organs were also examined for the distribution of probe **19** in the animal physiology post-i.v. injection, which indicates organs involved in metabolism and elimination have fluorescence signals, especially the liver and kidney (organ encircled with magenta and yellow dotted box), as shown in Fig. 10C.

To ascertain the test substance's BBB permeability, HPLC analysis was performed in ICR mice (22–24 g, male, n = 2) injected with a solution of probe **19** [DMSO: propylene glycol (25:75); 4 mg/kg]. The HPLC chromatograms confirmed the presence of maximum release of probe **19** in the brain region within 30 minutes, with a traceable amount of probe **19** detected in the brain homogenate extract at 60 min. It indicates that probe **19** has the propensity to enter the brain rapidly and has an effective clearance rate (Fig. S46, ESI†).

2.12 Aβ specific immunofluorescence and ThT costaining to evaluate probe efficiency in autopsy brain sections from elderly AD patients.

Encouraging results of histological fluorescence staining in brain sections from *APP/PS1* mice prompted us to revalidate the performance of leading probe **19** and **22** against Aβ aggregates in autopsy brain sections (10 µm) from elderly AD patients *via* immunofluorescence assay. Fluorescence activity was examined using confocal microscopy at different filters to observe specific amyloid-beta staining, nonspecific binding as well as the level of background staining with probes. Herein, probe **18** was also considered to perform the assay with the brain tissues to examine the sensitivity of probes upon varying the length of carbon spacer on rhodanine fragment. The staining with probe **18** was also found to be

nonspecific and with higher background signals (Fig. S48, ESI†). As shown by the staining pattern, we can conclude that probe **22** was found to have fluorescence in multiple filters with some nonspecific staining throughout the sections (Fig. S50, ESI†). The resultant finding is consistent with the staining data of *APP-PS1* mice brain data. Whereas, probe **19** was found to be more specific and sensitive to amyloid beta compared to probes **18** and **22**, furthermore, no apparent nonspecific binding was observed in the sections (Fig. S49, ESI†). Afterward, the colocalization study was performed using an anti-amyloid beta antibody (Fig. 11B&F) that recognizes oligomeric species of amyloid beta peptides, including $A\beta_{1-42}$ aggregates. We observed that probe **19** positively and selectively recognizes amyloid plaques and colocalizes with anti-amyloid beta antibody and less background than the anti-amyloid beta antibody, which offers better specificity. The integrated densities of ROIs (Aβ plaques, yellow stain in D&H of Fig. 11-I) also revealed that the amyloid β immunofluorescenc signals were correlated with the probe **19** signals with statistically non-significant difference in the intensities, as shown in Fig. 11-II. Collectively, the experimental data suggests that spacer length at rhodanine acceptor fragment may contribute to improve the affinity of probes towards amyloid beta species.

Similarly, probe **19** was incubated with autopsy brain tissue (hippocampal region, 15 µm) from AD and control patients and counterstain the same with ThT (widely used for selective *in-vitro* detection of amyloid beta aggregates) for mapping the position and distribution of Aβ plaques. Probe **19** and ThT (Fig. 12A-C) showed no apparent fluorescence staining pattern in the hippocampal brain tissue from control patients. Compared to this, both cored (yellow arrow with solid line) and diffuse plaques (yellow arrow with dotted line) could stained efficiently with probe **19** in the AD patient brain tissues (hippocampal region), which was further confirmed by counterstaining the same tissue slides with ThT dye as shown in images Fig. 12D-F. Intriguingly, overlap of fluorescence intensities (Fig. 12I) were observed in the signal intensity graph in the linear region of interest (ROI, cored plaques) across the white arrow line in images D, E, and F of Fig. 12, confirmed colocalization and also displayed slightly higher staining S/N ratio of probe **19** compared to the reference dye (Fig. 12G). These results were well consistent with the data obtained from immunofluorescence assays and confocal fluorescence imaging data (Fig. S51, ESI†). These staining results suggest that probe **19** could have higher selectivity and affinity for Aβ plaques with minimal background interference, a prerequisite criterion for histopathological staining.

2.13 Detection of Ocular Aβs deposits in developing eyes of the Drosophila AD model

At the molecular level, studies from the *Tg*-AD animal model and staining of autopsy samples from AD patients confirmed the existence of typical AD biomarkers (Aβ and Tau) inside the retina, which may serve as a surrogate marker of brain Aβ levels. Experimental data showed a quantitative relationship between retinal and cerebral Aβ loads in AD patients.(39, 40) In addition to the above factors, the retina can be imaged non-invasively and is more accessible for imaging than the brain, making it an ideal organ for optical imaging.(41) Therefore, we studied the levels of amyloid fibrils deposition in the developing eyes of the transgenic *UAS-$A\beta_{42}$/CyO* and the eye-specific *ey-GAL4/CyO* Drosophila strains.(42) Herein, ThT was used as a potent fluorescence marker of amyloid detection (a widely used Aβ-specific dye). It exhibits

strong green fluorescence in the eye's imaginal discs only when it is bound with amyloid fibrils. Contrarily, in the absence of amyloid deposits, the dye fluorescence faintly in the eye imaginal discs. The ThT exhibited weak fluorescence as observed in the control, while fluorescence intensity was increased in the presence of amyloid fibrils deposition in AD eye imaginal discs as shown in images A and B of Fig. 13(I). Similarly, leading probe **19** was used for amyloid detection pertaining to red fluorescence activity and demonstrated similar trends of fluorescence action corresponds to ThT. This study demonstrated that probe **19** labelled the existance of amyloid fibril aggregates in the form of tiny glitters in AD eye imaginal discs in images C and D of Fig. 13(II), whereas no apparent signals were observed in the eye discs of control fly as shown in images A and B of Fig. 13(II).These amyloid aggregates in eye imaginal discs are equivalent to the protein produced by the transgene during AD pathogenesis.

2.14 Ex-vivo histological staining of eye imaginal disc L3 larvae of Drosophila models

To further confirm fluorescence imaging efficacy, *ex-vivo* histological staining of eye imaginal disc from genetically modified (AD) L3 Drosophila larvae and wild-type L3 Drosophila larvae was performed upon feeding them with a 50 μM concentration of ThT, and probes of interest, i.e., **18**, **19**, and **22**. Interestingly, Fig. 14 showed that all the dyes exhibited intensified fluorescence signals in the eye imaginal disc of *Tg*-AD L3 Drosophila larvae relative to control fly larvae, which we presumed was due to the affinity of tested probes against Aβs. Contrary to this, the fluorescence intensity signals were moderate in control Drosophila L3 larvae. In the case of ThT staining (Fig. 14D, H), the *Tg*-AD fly eye disc fluorescence signals became saturated relatively to control fly staining, which confers the presence of amyloid beta load in the transgenic flies.

3. Dft Calculation And Molecular Docking Studies

3.1. DFT Calculation:

To better understand the intramolecular charge transfer, molecular orbitals of the probes are obtained using the Gaussian16. DFT calculation with B3LYP 6-31G (2d, p) basis sets were employed for this experiment. The only modification was done at the carbon space (n = 1–5) at the rhodanine fragment of the scaffold, which did not directly affect the transition and delocalization of π-electron in the resulting framework. Careful examination of HOMO shows that an electron cloud was spread throughout the molecule, while in LUMO, this cloud is slightly shifted toward the acceptor region of the molecule, validating the charge transfer delocalization phenomena in the D-π-A scaffold. The energy gap and the HOMO-LUMO energies are given in Fig. 15. Moreover, low energy gaps between these orbitals suggest the high reactivity of the developed probes.

3.2. Molecular Docking:

Blind docking was performed on Aβ42 filaments from human brains (PDB ID: 7Q4M)(43) to get the binding site profile of the probes using vina followed by analysis using the ADFR suite, Ligplot+, and Maestro. The docking experiment was repeated to obtain reproducible results. Best-docked conformers with their average scores and interacting amino acid residue were provided in Table 2. Molecular docking

of reference dye ThT(44) with the target protein revealed that it binds to four sites (OR two mirror sites). ThT shows preferential binding to site 3 (referred to as the ThT binding site; Fig. 16A), with an average score of -5.822. The best score generated on this site has a docking score of -6.076 as shown in the 2-D interaction diagram of Fig. 17A. Out of a hundred repeated docking, 97 times docking gives the best result on the ThT binding site. Probes show the binding at two different sites (probe binding sites, Fig. 16A) located between the two protofibrils, and these sites are mirror sites of each other. A closer look at the probe binding pocket (Site 1 or 2, Fig. 16B) revealed that Ala42, Ser26, and Lys28 are the most common interacting residues, although these residues are of different chains. The second or third solution of docking of ThT also shows binding toward the probe binding site. The best score on the probe binding site is -5.835, which is very close to the ThT binding site score, suggesting that ThT also shows binding affinity toward the probe binding site. The difference in the preference might be due to the small size of the reference molecule. Interestingly all the probes show the binding to the multiple chains simultaneously. It is possible because of their orientation inside the binding pocket where it can interact with multiple chains as shown in Fig. S52A-F of ESI†. In the case of ThT, pose from the Probe binding site was used to compare with Probes. ThT didn't show any hydrogen bonding, although hydrophobic interaction was present. Ligands **19** and **22** have average docking score values of -6.578 and − 6.446 kcal/mol, respectively, which is in close agreement with the K_d value (0.143 and 0.609 μM, respectively) determined using fluorescence saturation binding assay. All the docked probes (**18, 19, 22, 24**, and **26;** Table 2**)** have docking score values significantly lower than ThT, indicating that these probes might have better binding affinity to Aβ aggregates. 2-D interaction diagram revealed that the lactone ring of probe 19 displayed two hydrogen bond interactions with Ser26 (chain A) and causes planer alignment of the probe with the benzothiazole fragment of ThT (Fig. 16E), whereas the carbonyl group at rhodanine fragment form hydrogen bonding with Val24 (chain G) and Gly25 (chain A) and causes twisted geometry along the double bond extension. Similarly, probe **22** displayed two hydrogen bond interactions with Lys28 (chain B and J) and one with Ser26 (chain J) residue (Fig. 16D and 17C). These hydrogen bond interactions might be responsible for the higher affinity of the probe towards Aβ aggregated proteins, as shown in Fig. 16C-D and 17B-C.

Table 2
Docking Score and Interacting residues from the docking.

Ligand	Docking Score* (K)	Average Score†	Residues forming hydrogen bonds [Res(chain)]
18	-6.422	-6.165	Ser26(A)
19	-6.800	-6.578	Ser26(A), Gly25(A), Val24(G)
22	-6.820	-6.446	Lys28(J), Ser26(J), Lys28(B)
24	-7.012	-6.711	Ala42(H), Ser26(G), Lys28(A), Ala42(D)
26	-6.976	-6.719	Ala42(D), Lys28(A), Lys28(I), Ser26(I)
Thioflavin T	-5.835	-	None

*Lowest score from the hundred repeated docking, the pose that generated these scores were used for further analysis; †Average of hundred repeated docking of Model 1.

4. Conclusion

Amyloid beta and NFTs are the widely studied pathogenic biomarkers of AD. Consequently, several D-π-A-based NIRF probes are currently being developed that can be employed efficiently and selectively for detecting these AD markers in preclinical and clinical studies. In this work, new rhodanine composite coumarin and carbostyril-based fluorescent probes were rationally designed and biologically evaluated against the key AD marker proteins. All the probes demonstrated optimal optical profiles such as high stokes shift values and fluorescence emission maxima in the red to NIR range. In particular, coumarin-based dyes termed probe **19** showed encouraging results in *in-vitro* experiments, including optimal photophysical characteristics, a high binding affinity, low cytotoxicity, and acceptable photophysical and biostability. The spectra of probe **19** displayed an intensified fluorescence signal upon binding to Aβ aggregates, and emission maxima at the red region (635 nm), was very close to the best range of NIR imaging. Additionally, probe **19** also possesses an affinity for Tau aggregates with distinct fluorescent behaviors (25 nm blue shift in emission maxima). NIRF performance of probe **19** in *in-vitro* and *ex-vivo* studies strongly recommends labeling activity against amyloid beta species, equivalent to ThT, and a superior S/N ratio to eliminate background interference (Fig. 12G-I). Moreover, successful in-vivo brain imaging in living mice indicates efficient BBB permeability and acceptable brain kinetics of the leading probe. As a result of the probe's affinity for amyloid beta aggregates, in-silico investigations were done to study binding interactions with the misfolded Aβ protein, which showed Ser26 and Lys28 are the most common interacting amino acid residues within the binding cavity. This could benefit the development of a novel Aβ probe design. Overall, findings from our studies suggest that the coumarin-based probes have affinity and selectivity for AD marker proteins. However, more biological investigations are needed to determine the probes' potential for *in-vivo* preclinical and clinical use. We assume that the scaffold has the potential to be evolved as an efficient smart NIR probe for the detection of AD marker proteins.

5. Materials And Methods

5.1. General information

To develop novel NIRF probes, reaction progress was monitored on TLC chromatography on precoated silica gel 60 (Merck KGaA). Purifications were carried out using glass column chromatography with a stationary phase of silica gel (60–120 mesh size). ^{1}H NMR and HRMS were used for the structural elucidation of intermediates and desired probes. Fluorescence and absorption spectra were obtained using a fluorescence Microplate reader (Spectramax Paradigm, and i3x; Molecular devices, America). *In-vitro* and *ex-vivo* high-resolution fluorescence tissue images were recorded using LSM980 (Carl Zeiss) and Leica-LCS-SP8 laser confocal microscope integrated with commonly used filter sets (DAPI, FITC, and TRITC, etc.).

5.1.1. Synthesis of coumarin-based intermediates:

4-(Dimethylamino)-2-hydroxybenzaldehyde (2):

To a stirred solution of dry dimethyl formamide (DMF, 10.0 mL) at 0°C, 4.0 mL of phosphorus oxychloride ($POCl_3$) was added dropwise under an inert (nitrogen) atmosphere. Then, 3-(dimethylamino)phenol (**1**; 1.50 g, 10.93 mmol) was added in one portion to the resultant stirring mixture and allowed to stir at room temperature for 1 h followed by being heated at 70°C in an oil bath. On completion of the reaction (checked by TLC), the reaction mixture was poured slowly on to the crushed ice (100 g), and the resultant mass was extracted with ethyl acetate (EtOAc; 100.0 mL x 3). Finally, the combined organic phases were washed with ice-cold water (25.0 mL x 3), dried with anhydrous sodium sulfate, and concentrated under reduced pressure to afford 0.85 g of the target compound **2** as an off-white crystalline solid powder with a quantitative yield of 56.67%. It was used directly for the next step without column purification. ^{1}H NMR (500 MHz, $CDCl_3$): δ 11.62 (s, 1H), 9.54 (s, 1H), 7.30 (d, *J* = 9.0 Hz, 1H), 6.31 (dd, *J* = 9.0, 2.5 Hz, 1H), 6.10 (d, *J* = 2.5 Hz, 1H), 3.08 (s, 6H).

Ethyl 7-(dimethylamino)-2-oxo-2H-chromene-3-carboxylate (3):

To a stirred solution of compound **2** (0.85 g, 5.1 mmol) and diethyl malonate (1.64 g, 10.29 mmol) in EtOH (50.0 mL), 0.043 g piperidine (0.51 mmol) was added. The resulting red solution was heated at 100°C for 12 h. On complete consumption of compound **2** (checked by TLC), the resultant reaction mass was concentrated under reduced pressure followed by the addition of 25.0 mL chilled ice water. The solid thus precipitated was filter-out, washed with water (10.0 mL x 2), and dried under reduced pressure to obtain compound **3**. Finally, the crud precipitate was washed with cold ether (5.0 mL) to afford 0.650 g of the target compound (3) as a dark yellow crystalline solid powder with a quantitative yield of 48.50%. It was used directly for the next step without column purification. ^{1}H NMR (500 MHz, CDCl3) δ 8.45 (s, 1H), 7.39 (d, J = 8.9 Hz, 1H), 6.64 (dd, J = 8.9, 2.4 Hz, 1H), 6.47 (d, J = 4.9 Hz, 1H), 4.39 (q, J = 7.1 Hz, 2H), 3.13 (s, 6H), 1.40 (t, J = 7.1 Hz, 3H).

7-(Dimethylamino)-2H-chromen-2-one (4):

In a sealed tube, compound **3** (0.65 g, 2.48 mmol) was added to a 10 ml binary mixture of 35% strength of aq. hydrochloric acid and glacial acetic acid (AcOH) in a 1:1 ratio (v/v) and subjected to reflux at 125°C for 12 h. Upon completion of the reaction (checked by TLC), it was concentrated under reduced pressure and a solid mass was obtained. The crude residue was purified by column chromatography on silica (100–200 mesh) with 15–20% of EtOAc: hexene (v/v) as eluent to obtain 0.300 g (64%) of compound **4** as purple powder. ^{1}H NMR ($CDCl_3$, 500 MHz): δ 7.57 (d, *J* = 9.3 Hz, 1H), 7.28 (s, 1H), 6.61 (dd, *J* = 8.7, 1.6 Hz, 1H), 6.52 (d, *J* = 2.2 Hz, 1H), 6.08 (d, *J* = 9.3 Hz, 1H), 3.07 (s, 6H).

7-(Dimethylamino)-2-oxo-2H-chromene-3-carbaldehyde (5):

To a stirred solution of dry DMF (3.0 mL, 3.86 mmol) in a round-bottom flask under an ice-water bath environment, $POCl_3$ (1.5 mL) was added dropwise and allowed to stir at 0°C for 10 min. Then, the temperature was allowed to raise to room temperature. Thereafter, compound **4** (0.3 g, 1.58 mmol) was added to the resultant reaction mixture in one portion. The reaction mixture was allowed to stir at room temperature for 1 h, followed by heated at 75°C on an oil bath for another 4h. The reaction was monitored for complete consumption of compound **4**. On completion, the reaction mixture was poured slowly onto crushed ice (25.0 g), and a yellow solid was formed. Finally, the solid mass was washed thoroughly with water, dried, and rinsed with cold EtOH (2.0 mL) to afford 0.140 g of compound **5** as a pale-yellow solid powder with a quantitative yield of 40%. ^{1}H NMR (500 MHz, DMSO-d_6) δ 9.90 (s, 1H), 8.41 (s, 1H), 7.68 (d, *J* = 9.0 Hz, 1H), 6.82 (dd, *J* = 9.0, 2.3 Hz, 1H), 6.59 (d, *J* = 2.1 Hz, 1H), 3.12 (s, 6H).

5.1.2. Synthesis of carbostyril-based intermediates:

N-(3-(Dimethylamino)phenyl)acetamide (7):

To a stirred solution of 3-fluoroaniline (**6**; 2.5 g, 22.50 mmol) in dry DCM (25.0 mL), acetyl chloride (0.76 g, 27.00 mmol) was added dropwise over 15–20 min at 0°C followed by triethylamine (TEA; 2.7 g, 27.00 mmol). The temperature was raised to room temperature, and the reaction mixture was stirred at rt for 6 h. On completion, ice-chilled water (10.0 mL) was added to the reaction mixture and extracted with a 10% binary mixture of MeOH in DCM (50.0 mL x 3). The combined organic phase was dried over sodium sulfate and concentrated under reduced pressure to get 2.4 g of target compound **7** as a semisolid mass with a quantitative yield of 69.76%, which upon standing converted to a dark black crystalline solid. It was used directly for the next step without column purification.

2-Chloro-7-fluoroquinoline-3-carbaldehyde (8):

To a stirred solution of dry DMF (3.45 g, 47.01 mmol) at 0°C in a round bottom flask (100 mL capacity), $POCl_3$ (31.26 g, 195.87 mmol) was added dropwise under an inert atmosphere over 15–20 min. The reaction mixture was stirred as such under a nitrogen atmosphere for 1h. Then compound **7** (2.4 g, 15.67 mmol) was added in one portion. The temperature of the reaction mixture was allowed to be gradually

raised to 37°C, followed by being heated at 80°C in an oil bath. On complete consumption of starting material (7), the reaction mixture was poured slowly on crushed ice (100.0 g), the solid thus precipitated was filter-out, washed with water (10.0 mL x 2), and vacuum dry to get 1.74 g of target compound **8** as an off-white solid mass with a quantitative yield of 52.73%. It was used directly for the next step without column purification. ^{1}H NMR (500 MHz, $CDCl_3$) δ 10.55 (s, 1H), 8.76 (s, 1H), 8.01 (dd, *J* = 9.0, 5.9 Hz, 1H), 7.71 (dd, *J* = 9.6, 2.3 Hz, 1H), 7.45 (td, *J* = 8.8, 2.5 Hz, 1H).

7-Fluoro-2-oxo-1,2-dihydroquinoline-3-carbaldehyde (9):

To a suspended slurry of compound **8** (0.220 g, 10.52 mmol) in 25.0 mL of glacial AcOH, 5.0 mL water was added, and the resultant reaction mass was heated at 100°C for 12h. The temperature was reduced to 37°C, and the reaction was monitored for complete consumption of starting material. After the reaction was complete, the volume of the resulting mixture was reduced to a minimum under negative pressure, ice-chilled water (50.0 mL) was added to it, and then the pH of the resultant mass was adjusted with a NaOH solution (1.0 N) till white crystals get precipitated. The precipitate was filtered and its purification was done using silica gel (100–200 mesh) column chromatography with 2–5% MeOH in DCM as eluent to give 0.110 g (46%) of compound **9** as a white solid powder. ^{1}H NMR (500 MHz, d_6-DMSO) δ 12.31 (s, 1H), 10.21 (s, 1H), 8.53 (s, 1H), 8.03 (dd, *J* = 8.8, 6.2 Hz, 1H), 7.16 (td, *J* = 8.8, 2.5 Hz, 1H), 7.09 (dd, *J* = 10.2, 2.5 Hz, 1H).

7-(Dimethylamino)-2-oxo-1,2-dihydroquinoline-3-carbaldehyde (10):

To a stirred solution of 7-fluoro-2-oxo-1,2-dihydroquinoline-3-carbaldehyde (**9**; 0.100g, 5.23 mmol) in DMF (3.0 mL) was added dimethylamine hydrochloride (0.127g, 15.69 mmol) followed by anhydrous K_2CO_3 (0.289 g, 21mmol) and the reaction mass was heated at 110°C for 12 h in a sealed tube. The temperature was reduced to 37°C, and the reaction was monitored for complete consumption of starting material on TLC. On completion, the reaction mixture was poured slowly on crushed ice (50.0 g) and the pale-yellow solid precipitate formed was filtered to give 0.075 g of compound **10** with a quantitative yield of 85%. It was used directly for the next step without column purification. ^{1}H NMR (500 MHz, d_6-DMSO) δ 11.64 (s, 1H), 10.10 (s, 1H), 8.26 (s, 1H), 7.65 (d, J = 9.1 Hz, 1H), 6.77 (dd, J = 9.1, 2.4 Hz, 1H), 6.41 (d, J = 2.3 Hz, 1H), 3.07 (s, 6H).

5.1.3. General procedure for the synthesis of substituted rhodanine-based intermediates (13–17)

To a solution of compound **11a-e** (1.0 mmol) in 15 mL of 22% potassium hydroxide (KOH, 2.0 mmol) aqueous solution was added dropwise carbon disulfide (CS_2; 1.0 mmol), making sure that the temperature of the reaction mixture was not exceeded beyond 25°C. After stirring the reaction mixture at room temperature for approximately 3h, chloroacetic acid (1.0 mmol) was added portion-wise over 20 min. The reaction mixture was stirred at room temperature for an additional 16h, during which time a precipitate was formed. The pH of the reaction mixture was adjusted to 3–4 using concentrated H_2SO_4

and the precipitate thus formed was filtered off, and washed with water (15.0 mL x 3) to afford desired pure substituted rhodanine-based intermediates (13–17) with a quantitative yield of 40–65%.

2-(4-Oxo-2-thioxothiazolidin-3-yl) acetic acid (13):

The Intermediate **11a** (glycine; 3.0 g, 40 mmol), was treated with 22% KOH (4.48 g, 80 mmol), CS_2 (3.045 g, 40.0 mmol), and chloroacetic acid (3.799 g, 40.0 mmol) using the experimental protocol described above to afford 3.2 g of pure target compound **13** as a pale yellow solid crystalline powder with a quantitative yield of 40%. ^{1}H NMR (500 MHz, d_6-DMSO): δ 13.32 (s, 1H), 4.57 (s, 2H), 4.42 (s, 2H).

3-(4-Oxo-2-thioxothiazolidin-3-yl) propanoic acid (14):

For the synthesis of compound **14** from Intermediate **11b** (β-alanine; 3.0 g, 33.70 mmol), the same experimental protocol was followed as for compound **13.** After completion of the reaction, we obtained 3.0 g of pure compound **14** as a light pinkish crystalline powder with a quantitative yield of 44%. ^{1}H NMR (500 MHz, d_6-DMSO) δ 12.49 (brs, 1H), 4.23 (s, 2H), 4.06 (t, J = 8.0 Hz, 2H), 2.53 (t, J = 8.0 Hz, 2H).

4-(4-Oxo-2-thioxothiazolidin-3-yl)butanoic acid (15):

For the synthesis of compound **15** from Intermediate **11c** (4-aminobutanoic acid; 3.0 g, 29.10 mmol), the same experimental protocol was followed as for compound **13.** After completion of the reaction, we obtained 3.85 g of pure compound **15** as a light pink crystalline powder with a quantitative yield of 60%. ^{1}H NMR (500 MHz, d_6-DMSO): δ 12.11 (s, 1H), 4.23 (s, 2H), 3.91 (t, J = 7.0 Hz, 2H), 2.26 (t, J = 7.4 Hz, 2H), 1.77–1.83 (m, 2H).

5-(4-Oxo-2-thioxothiazolidin-3-yl)pentanoic acid (16):

For the synthesis of compound **16** from Intermediate **11d** (5-aminopentanoic acid; 3.0 g, 25.61 mmol), the same experimental protocol was followed as for compound **13**. After completion of the reaction, we obtained 2.85 g of pure compound **16** as a light pinkish crystalline powder with a quantitative yield of 48%. ^{1}H NMR (500 MHz, d_6-DMSO): δ 12.08 (s, 1H), 4.25 (s, 2H), 3.85 (t, J = 7.2 Hz, 2H), 2.23 (t, J = 7.2 Hz, 2H), 1.60–1.55 (m, 2H), 1.54–1.47 (m, 2H).

6-(4-Oxo-2-thioxothiazolidin-3-yl) hexanoic acid (17):

For the synthesis of compound **17** from Intermediate **11e** (6-aminohexanoic acid; 3.5 g, 26.68 mmol), the same experimental protocol was followed as for Intermediate **13**. After completion of the reaction, we obtained 4.20 g of pure compound **17** as a light orange crystalline powder with a quantitative yield of 64%. ^{1}H NMR (500 MHz, d_6-DMSO): δ 12.07 (s, 1H), 4.23 (s, 2H), 3.85–3.82 (m, 2H), 2.19 (t, J = 7.4 Hz, 2H), 1.57–1.47 (m, 4H), 1.32–1.23 (m, 2H).

5.2. Novel probes synthesis and characterization:

The general synthesis procedure used Knoevenagel condensation reaction conditions, in which corresponding aldehyde **5** (Scheme 1) or **10** (Scheme 2) was reacted with rhodanine intermediates (**13–17;** Scheme 3) in absolute ethanol and piperidine at 110°C in an RBF with continuous stirring for 12-16h under nitrogen atmosphere. The excess solvent was removed under vacuum, and the resulting crude residues were purified using silica gel column chromatography using a gradient of MeOH in DCM (1–5%) as eluent, following crystallization in cold MeOH to afford desired probes in a quantitative yield of 20–35%.

5.2.1. (Z)-2-(5-((7-(Dimethylamino)-2-oxo-2H-chromen-3-yl)methylene)-4-oxo-2-thioxothiazolidin-3-yl)acetic acid (I-16, 18):

Piperidine (0.015 g, 0.172 mmol; approximately 2–3 drops) was added to a stirring mixture of compound **5** (0.100 g, 0.46 mmol) and **13** (0.131 g, 0.69 mmol) in absolute ethanol (15 mL). The reaction mixture was then treated as specified in the general procedure. The purification of crude material was done using silica gel (100–200 mesh size) column chromatography as a stationary phase and MeOH in DCM (1–3%) as eluent to afford 0.045 g (25%) of target dye **I-16** (18) as a dark brick-red amorphous powder.

5.2.2. (Z)-3-(5-((7-(Dimethylamino)-2-oxo-2H-chromen-3-yl)methylene)-4-oxo-2-thioxothiazolidin-3-yl)propanoic acid (I-8, 19):

Compound **19** was synthesized from compound **5** (0.100 g, 0.46 mmol) and **14** (0.141 g, 0.69 mmol), in absolute ethanol (10 mL) followed by the general procedure as described above for compound **18**. The purification of crude material was done using silica gel (100–200 mesh size) column chromatography as a stationary phase and MeOH in DCM (1–3%) as eluent to afford 0.045 (22%) g of desired dye **I-8** (19) **as a** dark reddish-brown amorphous powder.

5.2.3. (Z)-4-(5-((7-(Dimethylamino)-2-oxo-2H-chromen-3-yl)methylene)-4-oxo-2-thioxothiazolidin-3-yl)butanoic acid (I-17, 20):

Compound **20** was synthesized from compound **5** (0.100 g, 0.46 mmol) and **15** (0.151 g, 0.69 mmol), in absolute ethanol (10 mL) followed by the general procedure as described above for compound **18**. The purification of crude material was done using silica gel (100–200 mesh size) column chromatography as a stationary phase and MeOH in DCM (1–3%) as eluent to afford 0.055 (29%) g of targeted dye **I-17** (20) as a dark reddish-brown amorphous powder.

5.2.4. (Z)-5-(5-((7-(Dimethylamino)-2-oxo-2H-chromen-3-yl)methylene)-4-oxo-2-thioxothiazolidin-3-yl)pentanoic acid (I-18, 21):

Compound **21** was synthesized from compound **5** (0.100 g, 0.46 mmol) and **16** (0.161 g, 0.69 mmol), in absolute ethanol (10 mL), followed by the general procedure as described above for compound **18**. The purification of crude material was done using silica gel (100–200 mesh size) column chromatography as a stationary phase and MeOH in DCM (3–5%) as eluent to afford 0.045 (23%) g of targeted dye **I-18** (21) as a dark reddish-brown amorphous powder.

5.2.5. (Z)-6-(5-((7-(Dimethylamino)-2-oxo-2H-chromen-3-yl) methylene)-4-oxo-2-thioxothiazolidin-3-yl)hexanoic acid (I-3, 22):

Compound **22** was synthesized from compound **5** (0.150 g, 0.69 mmol) and **17** (0.256 g, 1.035 mmol) in absolute ethanol (10 mL), followed by the general procedure as described above for compound **18**. The purification of crude material was done using silica gel (100–200 mesh size) column chromatography as a stationary phase and MeOH in DCM (3–5%) as eluent to afford 0.060g (21%) of desired dye **I-3** (22) as a dark reddish amorphous powder.

5.2.6. (Z)-2-(5-((7-(Dimethylamino)-2-oxo-1,2-dihydroquinolin-3-yl)methylene)-4-oxo-2-thioxothiazolidin-3-yl)acetic acid (I-22, 23):

Compound **23** was prepared by condensation of compound **10** (0.100 g, 0.46 mmol) and **13** (0.131 g, 0.69 mmol) in absolute ethanol (10 mL), according to the general procedure mentioned above for compound **18**. The crude was purified by column chromatography (100–200 mesh size) using DCM/MeOH gradient system (3–4% MeOH) as eluent to afford 0.045 g (25%) of desired compound **I-22** (23) as a dark brick-red amorphous powder.

5.2.7. (Z)-3-(5-((7-(Dimethylamino)-2-oxo-1,2-dihydroquinolin-3-yl)methylene)-4-oxo-2-thioxothiazolidin-3-yl)propanoic acid (I-20, 24):

Compound **24** was prepared by condensation of compound **10** (0.100 g, 0.46 mmol) and **14** (0.141 g, 0.69 mmol) in absolute ethanol (10 mL), according to the general procedure described above for compound **18**. The crude was purified by column chromatography (100–200 mesh size) using DCM/MeOH gradient system (3–5% MeOH) as eluent to afford 0.045 g (30%) of desired dye **I-20** (24) as a dark reddish-brown amorphous powder.

5.2.8. (Z)-4-(5-((7-(Dimethylamino)-2-oxo-1,2-dihydroquinolin-3-yl)methylene)-4-oxo-2-thioxothiazolidin-3-yl)butanoic acid (I-12, 25):

Compound **25** was prepared by condensation of compound **10** (0.100 g, 0.46 mmol) and **15** (0.151 g, 0.69 mmol) in absolute ethanol (10 mL), according to the general procedure described above for

compound **18**. The crude was purified by column chromatography (100–200 mesh size) using DCM/MeOH gradient system (3–5% MeOH) as eluent to afford 0.040 g (21%) of desired dye **I-12** (26) as a dark reddish-brown amorphous powder.

5.2.9. (Z)-5-(5-((7-(Dimethylamino)-2-oxo-1,2-dihydroquinolin-3-yl)methylene)-4-oxo-2-thioxothiazolidin-3-yl)pentanoic acid (I-21, 26):

Compound **26** was prepared by condensation of compound **10** (0.100 g, 0.46 mmol) and **16** (0.161 g, 0.69 mmol) in absolute ethanol (10 mL), according to the general procedure described above for compound 18. The crude was purified by column chromatography (100–200 mesh size) using DCM/MeOH gradient system (3–5% MeOH) as eluent to afford 0.055 g (28%) of desired dye **I-21** (26) as a dark reddish-brown amorphous powder.

5.2.10. (Z)-6-(5-((7-(Dimethylamino)-2-oxo-1,2-dihydroquinolin-3-yl)methylene)-4-oxo-2-thioxothiazolidin-3-yl)hexanoic acid (I-10, 27):

Compound **27** was prepared by condensation of compound **10** (0.150 g, 0.69 mmol) and **17** (0.256 g, 1.035 mmol) in absolute ethanol (10 mL), according to the general procedure described above for compound 18. The crude was purified by column chromatography (100–200 mesh size) using DCM/MeOH gradient system (1–3% MeOH) as eluent to afford 0.050 g of desired dye **I-10** (27) as a dark reddish-brown amorphous powder.

5.2. Photophysical spectroscopic measurements:

The absorption and fluorescence (Fig. S33-39 and Table S2.) spectrum of the probes were measured using a spectrophotometer at a gradient concentration of 4 to 20 μM in DMSO to determine the linear fit curve data and molar absorption coefficient ( ) values.
Briefly, the excitation and emission wavelengths of the developed molecules were performed as follows, 2.5 mM stock solutions of the test probe were prepared in DMSO, which was further diluted to prepare gradient concentrations such as 4, 5, 10, 15, and 20 μM of the test compounds in DMSO. All the spectral data were plotted using Origin Pro 9.0 software (OriginLab, Northampton, Massachusetts, USA).

5.2.1 Quantum yield determination:

The relative Quantum Yield (Φ_f) was determined using well-characterized reference samples with known Φ_f values. It is a simple ratio of the integrated fluorescence intensities of the test compound relative to the reference dye. The probes and references were dissolved in Dimethyl Sulfoxide (DMSO). The five different dilutions of probes and references were made with absorption values between 0.01 to 0.1 to minimize reabsorption effects. The absorbance & fluorescence were taken in a 10mm Cuvette. The integrated area of each fluorescence peak was calculated by Origin Pro software 9.0 (OriginLab). The graphs were plotted

as the integrated area of fluorescence intensity vs. absorbance of probes and reference. The straight line with gradient & intercept plot was generated.

$Q = Q_{(r)} \times (m/m_r) \times (\eta^2/ \eta_r^2)$

Here, Q and $Q_{(r)}$ denotes the quantum yield of probes and reference, respectively; m and m_r are gradients from the plot of integrated fluorescence intensity *vs.* absorbance of probes and reference, and η is the solvent's refractive index. The Quantum yield [$Q_{(r)}$] of Rhodamine B in DMSO is 0.44. Compound & reference solutions were prepared in DMSO, therefore $(\eta^2/ \eta_r^2) = 1$.

5.3. Biology

5.3.1. Preparation and quantification of Aβ1–42 fibrillar aggregates:

Amyloid β (Aβ) protein fragment 1–42 (CAS Number 107761-42-2) was purchased from rPeptide. All the experiments were performed in phosphate buffer saline (PBS) (10 mM, pH = 7.4). All the stock concentrations of the test and reference sample were prepared in molecular biology grade dimethyl sulfoxide (DMSO), and final dilutions were made in 10 mM PBS at pH 7.4. The stock solution was kept at − 78°C. For the $A\beta_{1-42}$ aggregation experiment, the Aβ stock solution was diluted with PBS (pH 7.4) to 25 μM before use. The $A\beta_{1-42}$ working concentration (1.769 mM) was estimated through the NanoDrop™ 2000/2000c spectrophotometer (Thermo Scientific instrument).

Thioflavin T (ThT) dye was used to quantify the formation of amyloid fibrils. A mixture of the peptide $A\beta_{1-42}$ (30 μL, 25 μM) with or without the ThT dye (30μL, 50 μM final concentration in ratio 1:2) was incubated on an Eppendorf thermo mixture C with the condensation-prevention top (Eppendorf, catalog No. 5382000015) with agitation at 300 rpm, at 37°C for 30 min. Next, the fluorescent emission spectra were measured by a fluorescence spectrophotometer with an excitation wavelength of 445 nm. The solvents with only PBS as blank control, ThT (50 μM) in PBS, and ThT (50 μM) with $A\beta_{1-42}$ (25 μM) of stock solution at 0-time point [Aβ (monomers)] were also measured in the same conditions. Fig. S40 indicated that samples incubating for 72 h on an Eppendorf Thermo mixture C with the condensation-prevention top (Eppendorf, catalog No. 5382000015) with agitation at 1200 rpm at 37°C shows a 7–8 folds increase in the fluorescence intensity of ThT compared to the sample containing ThT alone and ThT with Aβ (monomers), which confers formation of fibrils.

5.3.2. Fluorescence spectral assessment of developed probes with $A\beta_{1-42}$ and BSA:

Serum albumin is the most abundant plasma protein; therefore, it is crucial to determine the affinity of designed probes toward these proteins or not. To the solutions of test probes (30 μL, 50 μM) in PBS (pH = 7.4) was added $A\beta_{1-42}$ (30 μL, 25 μM) peptide suspension in PBS (pH = 7.4) or a 30μL solution of BSA in PBS of 50μg/mL stock solution. The probe vs. $A\beta_{1-42}$ peptide was taken in a ratio of 2:1 in the final

solution mixture. The mixture was incubated at 37°C with gentle and constant shaking (300 rpm) for 1.0 h. Then, the mixture was transferred to a 384-well plate black (n = 3), and the plate was subjected to fluorescence imaging using (BioTek Synergy H1M) fluorescence spectrophotometer. The spectra of the tested probes in PBS and of PBS buffer (as a blank control) were also measured using the same parameters. The fluorescence characterization of tested probes was determined using excitation wavelength (λ_{ex}) 520 nm to record spectral graphs over a range of 550–700 nm with a slit width of 5 or 10 nm.

5.3.3. Preparation of Tau fibrillar species [Tau (72)] from monomeric Tau species [Tau (0)]:

We adopted a well-known protocol for Tau aggregation with slight modification.(45) Tau protein stock solution (50 μM) was diluted to 21.79 μM (60 μL) with assembly buffer (10mM HEPES buffer containing 7.7mg of DTT and 58.44mg of NaCl). 108.9 μM solution of heparin (3 μL) was added to the tau preparation as an aggregation inducer. Tau protein's final concentration was (19.8 μM), and the final heparin concentration was 4.95 μM. The sample was incubated for 72 h at 37°C. Aggregation was confirmed *via* ThT fluorescence assay.

5.3.4 In-vitro **Aβ aggregates binding constant assay of the probes with promising data against Aβ1–42 fibrillar species**:

To a suspension of $A\beta_{1-42}$ aggregates (5 μM final concentration) in PBS (pH 7.4) was added gradient concentrations of probe **19** and **22**, ranging from 2.5 to 0.0075μM in the final assay mixture. All assay mixtures were incubated at 37°C with slight and constant shaking (300 rpm) for 1.0 h. Next, the solutions were transferred to black 384-well Costar assay plates (n = 3). The fluorescence intensity was recorded using BioTek Synergy H1M fluorescence spectrophotometer at 650 nm and 640 nm, respectively, using an excitation wavelength of 520 nm. Fluorescence intensity values of each probe were plotted versus their concentrations, and the binding constants were calculated using GraphPad Prism 8.0 (nonlinear regression, one site-binding).

5.3.5. pH-dependent fluorescence stability testing of the promising probes (18, 19, and 22):

The photostability of selected probes (18, 19, and 22) were tested in PBS buffer solutions at different pH ranges, such as 6.0, 6.7, 7.0, and 7.4. Solutions of the test probes (50 μM) at the above pH range were added to a 96-well plate (n = 5 for each pH and 2% DMSO co-solvent). Then the plate was subjected to fluorescence recording using BioTek Synergy H1M microplate reader after different incubation times (0, 5, 10, 30, 60, and 1440 min) at 37°C. The fluorescence data of the tested probes were recorded at their respective excitation and emission maxima. The excitation wavelength for all the tested probes (18, 19, and 22) was (λex) 520 nm, whereas emission maxima (λ_{em}) were recorded at 650, 640, and 630 nm, respectively. The signals at different time points were normalized to the signal at 0 min incubation for quantification.

5.3.6. Assessment of cell viability in PC12 cells

The cytotoxicity of probe **18**, **19**, and **22** in PC12 cells was determined by 3-(4, 5-dimethylthiazolyl-2)-2,5-diphenyltetrazolium bromide (MTT) assay. PC12 cells were differentiated with NGF-β (75 ng/ml) (H9666, Sigma) for 5–6 days before the experiment. Cells were seeded at 1×10^4 cells/well in 96 well plates and incubated overnight for adherence. The probes (18, 19, and 22) were added at a concentration of 0.1, 1, 2.5, 5, 10, and 20 μM and incubated for 24 h at 5% CO_2 at 37°C. The MTT reagent (0.5mg/ml) (T0793, BioBasic) was added and incubated for 3 hours at 37°C, formazan crystals were dissolved by DMSO, and the reading was taken at 562 nm on SpectraMax-i3x (Molecular Devices). The percentage of cell viability was calculated as $[OD_{(treated)}/ OD_{(Control)}]\times100$.

5.3.7. Stability study in the ICR mice plasma

The optimal plasma stability is essential for effective *in-vivo* efficacy; therefore, a plasma stability study of lead probes was performed in ICR mice plasma at various time points (0, 10, and 30 min). The mice serum (300 μL) was incubated with a 50 μL solution of **19** and **22** (50 μM) at 37°C. Acetonitrile (500 μL) was added, and the mixture was centrifugated at 7000 rpm for 15 min. The temperature was 4°C. The proteins in the plasma were precipitated, and the supernatant was collected. 0.1 mL of the supernatant was detected by HPLC (UV detector, λ = 510 nm).

5.3.8. Cell internalization:

The cell internalization of **18**, **19**, and **22** probes was tested in the PC12 cells. Cells were grown in glass bottom plates (FIS12-567-401, Thermo Scientific Nunc) and differentiated using Nerve Growth Factor-β human (75 ng/ml) (H9666, Sigma) for 5 days. Following differentiation, cells were treated with different concentrations of these probes (1 μM, 5 μM, and 10 μM; Fig. S47) and incubated for 40 minutes at 37°C in the dark. The plate containing probe-treated cells was imaged with Zeiss LSM980 Confocal Microscope (Carl Zeiss).

5.3.9. *In-vitro* fluorescence imaging of autopsy brain tissues:

All the autopsy neurological staining was performed after getting approval from the Institute Ethics Committee, AIIMS, New Delhi, India-110029, with Ref. No. **IEC-749/02.09.2022, RP-20/2022**, and Institute of Medical Science, BHU, Varanasi, India-221005 with Ref. No. **ECR/526/Inst/UP/2014/RR-20 dt. 19.5.2022**. The hippocampus from aged autopsy brains was collected, and fixed with 10% neutral buffered formalin, then cryoprotected in successive treatments of 15% and 30% sucrose buffered solutions. 20μm thick sections were taken using a cryostat (Microm, Thermofisher) and stored in 0.1M phosphate buffer with 0.1% sodium azide at 4°C till further processing. For Aβ staining with the probes (18, 19, and 22), the sections were treated with permeabilization buffer (PBS with 0.1% Triton X100) for 30 min at RT. Following permeabilization, the sections were stained with 20 μM of the probes in PBS at RT for 1 h and were mounted using Fluoroshield with DAPI (Sigma). For colocalization experiments, the

sections were labeled with rabbit polyclonal anti-amyloid beta oligomer (A11) (AHB0052, Invitrogen) primary antibody overnight at 4°C (1:200), followed by goat anti-rabbit-Alexa Fluor 488 secondary antibody (1:500, Jackson Immunoresearch) at RT for 2 h. The sections were counterstained with 20 μM of the probes in PBS at RT for 1 h and were mounted as described above. The images were collected using Zeiss LSM980 Confocal microscope (Carl Zeiss).

For ThT-based fluorescence imaging of formalin-fixed brain tissue slices were done as reported protocol. (30) Briefly, the tissue slides were cleansed by soaking them in xylene for 10 min twice before being rehydrated with 100% ethanol for 10 min, 95% ethanol for 5 min, 75% ethanol for 5 min, 50% ethanol for 5 min, 30% ethanol for 5 min, 0.85% NaCl for 3 min, and 10% for PBS, sequentially. The slices were then incubated for 5 min at room temperature in an aqueous solution of freshly prepared ThT 0.5% (g/mL), followed by washing with ethanol/water (v/v = 1:1) and PBS buffer (pH = 7.4) for 10 min. The slices were then counterstained for 20 minutes at room temperature in aqueous solutions of **19** (20 μM, 2.0% DMSO as co-solvent), following washed sequentially in 30% ethanol (3 min), 50% ethanol (2 min), 30% ethanol (2 min) and submerged in water for 10 min. Finally, slides were submerged in PBS for 20 min and covered with cover glasses prior to fluorescence observation using fluorescence (NIS-Elements BR 4.30.00.64-bit fluorescence microscope) & confocal microscope (Carl Zeiss microscope).

Paraffin-embedded 10 μm brain tissue sections from *APP/PS1* transgenic mouse (C57BL6, APP/PS1, 14 months old, male) was used for *in-vitro* fluorescent staining. Before staining, the slices were deparaffinized by washing with ethanol for 5 mins after 15 mins immersion in xylene. After washing with 50% ethanol, DD water and PBS buffer (pH = 7.4) respectively, the slices were incubated in aqueous solution of each probe (10 μM) for 30 mins at room temperature and then washed with ethanol/water (v/v = 50%:50%) followed by washing with PBS buffer (pH = 7.4). After removing the residual liquid with dust free paper, the slice was co-stained with 1% Thioflavin T (30% ethanol solution) for 10 mins. Next, the slice was covered with VectaShield mounting media. Florescence images were observed using Olympus VS200 microscope.

5.3.10. NIR *in-vivo* imaging and BBB permeability assay:

The 13-month-old *APP/PS1* (*Tg*-AD) and aged matched normal C57BL/6 wild-type (WT) mice were (n = 3) shaved to remove scalp hair before background imaging and were systemically injected with 100 μL of probe **19** (0.8 mg/kg; 15% of DMSO, 5% of Cremophor® EL, and 80% of 1X PBS) via the tail vein route. The NIR imaging paradigm was performed on LAGO X (Spectral Instruments Imaging). For *ex vivo* imaging studies, the mice were sacrificed at 20 min post *i.v.* injection, perfused with 4% paraformaldehyde (PFA) solution following 1x PBS, and excised to remove intact brain and vital organs (liver, heart, kidney and spleen) to examine the biodistribution of probe. For both the *in-vivo* and *ex vivo* imaging studies, images were acquired with a 500 nm excitation filter and a 620 nm emission filter. The acquisition and analysis of the data were performed using Aura Analysis Software. During the *in-vivo* imaging process, the mice were kept on the imaging stage under deep state of anesthesia acquired using ketamine-xylazine (75 mg/kg; 85:15 in saline) that lasted for about 120 minutes.

Blood-Brain Barrier (BBB) penetration efficacy of lead probes: A solution of probe **19** (25% DMSO and 75% propylene glycol, 100µL, 4 mg/kg) was injected *via* the tail vein of ICR mice (22–24 g, male). The mice brains were excised at representative time points (10, 20, 30 and 60 min) post-injection and homogenized with 1.0 mL PBS. Thereafter, the homogenate was centrifuged at 2,500 rpm for 5 min and the supernatant was separated. The leftover homogenate was extracted with 1.0 mL acetonitrile twice. The volume of the ACN was reduced to a minimum and again diluted with 250 µL of ACN. The extracts were filtered by flashing nylon membrane (0.22 µm) and analyzed using HPLC. HPLC conditions: acetonitrile/water (90/10, v/v) at a flow rate of 1.0 mL/min. The UV-detector was set for the probe **19** at 510 nm.

5.3.11 In-vitro **and** ex-vivo **imaging in the Drosophila AD model**

For *in-vitro* fluorescence imaging of leading probe staining and Thioflavin-T (ThT) as Aβ specific dye, staing protocol was performed with minor changes as per the method described previously by Beriault and Werstuck, 2013.(46) Both the transgenic *UAS-Aβ_{42}/CyO* and the eye-specific *ey-GAL4/CyO* Drosophila strains used in the research were obtained from the Bloomington Stock Center in Indiana, USA. The *ey-GAL4/CyO* male flies were crossed with virgin *UAS-Aβ_{42}/CyO* female flies to develop F1 progeny *ey-GAL4-UAS-Aβ_{42}/CyO* for AD phenotype. Aged matched fruit flies *ey-GAL4/CyO* as control and *ey-GAL4-UAS-Aβ_{42}/CyO* as Alzheimer's disease (AD) group were cultured in standard corn media in a BOD incubator at 28 ± 1^{o}C. Their F1 progeny 3rd instar larvae were dissected in 1xPBS (pH 7.4) through a fresh fine needle under stereozoom microscope to acquire the imaginal eye discs. The imaginal discs were washed with 1xPBS and subsequently fixed with fixative 4.0% paraformaldehyde for 15 minutes at room temperature (RT). The discs were rinsed with 1xPBS containing 0.2% TritonX-100 for 10 minutes at RT and incubated with 10 µM ThT (Sigma-Aldrich) and 10 µM solution of probe **18** and **19** in 50% ethanol for 60 minutes at RT in a dark, humid chamber. Eye imaginal discs were washed twice with 1xPBS and mounted in DABCO, followed by fluorescence imaging under a Zeiss LSM 780 confocal microscope.

For *ex-vivo* fluorescence imaging, the *Drosophila* L3 larvae were fed upon 50 µM solution of probe **18**, **19**, **22** and **ThT** in agar plates supplemented with yeast for two hours. The L3 larvae of each group were dissected in PBS with a fine needle and fixed the tissues in 4.0% paraformaldehyde for 20 minutes. The tissues were washed twice with 1xPBS and mounted in DABCO, then observed under fluorescence microscope (BR-elements).

5.3.12 DFT Calculation and computational studies:

QM methodology

TD-DFT calculations were used to understand the probe's spectral characteristics using Gaussian16(47, 48) program. DFT calculations were done to optimize the ground state geometry of probes using the B3LYP 6-31G (2d, p) basis set. Further optimized ground state structures were used to perform TD-DFT calculation. The calculations were performed in a vacuum. Negative frequencies were avoided to get ground state optimized geometry.

Computational studies:

1) Protein Preparation:

The crystal structure of amyloid-beta was obtained from the PDB database. The structure with PDB ID: 7Q4M(43) was selected for study as it had oligomeric form with a 2.80 Å resolution. It was prepared using the protein preparation wizard of the maestro. Using this tool, the hydrogens were added, water was removed (if any), converted selenomethionines to methionine, and added missing side chains and loops. The structure was optimized by propka at pH 7.0. Finally, restrained minimization was performed till heavy atoms converged to RMSD of 0.30 Å using the OPLS4 force field. Further, the structure was improved via the prepare_recepter script provided with the ADFR suit, where Gasteiger charges were added, and the final structure was obtained in pdbqt format.

2) Ligand Preparation:

The structures were drawn and optimized using Gaussian16. For optimization, B3LYP 6-31G(2d,p) level of theory was used. These structures were then passed to the prepare_ligand script, which is provided with ADFR suit(49, 50). It gave output in PDBQT format. In the case of ThT, structure was obtained from the PubChem database and prepared using the LigPrep(51) followed by the prepare_ligand script.

3) Molecular Docking:

An autodock vina(50, 52) program was used to perform docking. 56.250 * 75.000 * 36.000 were X, Y and Z coordinates of grid box for docking. Exhaustiveness was kept at 32 for maximum accuracy. The same docking was repeated hundred times, each time with a different seed. This approach helped choose the right binding site; the best binding pose was analyzed. Manual analysis was done using Ligplot+(53) and Maestro.

Declarations

Declaration of competing interest: The authors declare that there is no conflict of interest.

Data and materials availability: All data needed to evaluate the conclusions in the paper are present in the paper and/or the Supplementary Materials.

References

1. M. Ishii, C. Iadecola, Metabolic and Non-Cognitive Manifestations of Alzheimer's Disease: The Hypothalamus as Both Culprit and Target of Pathology. *Cell Metab.* **22**, 761-776 (2015).
2. J. Viña, A. Lloret, Why women have more Alzheimer's disease than men: gender and mitochondrial toxicity of amyloid-beta peptide. *J. Alzheimers Dis.* **20 Suppl 2**, S527-533 (2010).
3. I. T. Lott, M. Dierssen, Cognitive deficits and associated neurological complications in individuals with Down's syndrome. *Lancet Neurol* **9**, 623-633 (2010).

4. T. H. Ferreira-Vieira, I. M. Guimaraes, F. R. Silva, F. M. Ribeiro, Alzheimer's disease: Targeting the Cholinergic System. *Curr. Neuropharmacol.* **14**, 101-115 (2016).
5. Y. P. Singh, G. N. V. C. Tej, A. Pandey, K. Priya, P. Pandey, G. Shankar, P. K. Nayak, G. Rai, A. G. Chittiboyina, R. J. Doerksen, S. Vishwakarma, G. Modi, Design, synthesis and biological evaluation of novel naturally-inspired multifunctional molecules for the management of Alzheimer's disease. *Eur. J. Med. Chem.* **198**, 112257 (2020).
6. J. Yang, J. Yang, S. H. Liang, Y. Xu, A. Moore, C. Ran, Imaging hydrogen peroxide in Alzheimer's disease via cascade signal amplification. *Sci. Rep.* **6**, 35613 (2016).
7. S. Manoharan, G. J. Guillemin, R. S. Abiramasundari, M. M. Essa, M. Akbar, M. D. Akbar, The Role of Reactive Oxygen Species in the Pathogenesis of Alzheimer's Disease, Parkinson's Disease, and Huntington's Disease: A Mini Review. *Oxid. Med. Cell Longev.* **2016**, 8590578-8590578 (2016).
8. J. Yang, X. Zhang, P. Yuan, J. Yang, Y. Xu, J. Grutzendler, Y. Shao, A. Moore, C. Ran, Oxalate-curcumin-based probe for micro- and macroimaging of reactive oxygen species in Alzheimer's disease. *Proc. Natl. Acad. Sci. U. S. A.* **114**, 12384-12389 (2017).
9. T. J. Eckroat, A. S. Mayhoub, S. Garneau-Tsodikova, Amyloid-β probes: Review of structure–activity and brain-kinetics relationships. *Beilstein J. Org. Chem.* **9**, 1012-1044 (2013).
10. H. Akiyama, S. Barger, S. Barnum, B. Bradt, J. Bauer, G. M. Cole, N. R. Cooper, P. Eikelenboom, M. Emmerling, B. L. Fiebich, C. E. Finch, S. Frautschy, W. S. Griffin, H. Hampel, M. Hull, G. Landreth, L. Lue, R. Mrak, I. R. Mackenzie, P. L. McGeer, M. K. O'Banion, J. Pachter, G. Pasinetti, C. Plata-Salaman, J. Rogers, R. Rydel, Y. Shen, W. Streit, R. Strohmeyer, I. Tooyoma, F. L. Van Muiswinkel, R. Veerhuis, D. Walker, S. Webster, B. Wegrzyniak, G. Wenk, T. Wyss-Coray, Inflammation and Alzheimer's disease. *Neurobiol. Aging* **21**, 383-421 (2000).
11. P. R. Bharadwaj, A. K. Dubey, C. L. Masters, R. N. Martins, I. G. Macreadie, Abeta aggregation and possible implications in Alzheimer's disease pathogenesis. *J. Cell Mol. Med.* **13**, 412-421 (2009).
12. M. Shimojo, M. Higuchi, T. Suhara, N. Sahara, Imaging Multimodalities for Dissecting Alzheimer's Disease: Advanced Technologies of Positron Emission Tomography and Fluorescence Imaging. *Front. Neurosci.* **9**, 482 (2015).
13. J. Cao, B. Zhu, K. Zheng, S. He, L. Meng, J. Song, H. Yang, Recent Progress in NIR-II Contrast Agent for Biological Imaging. *Front Bioeng. Biotechnol.* **7**, 487 (2019).
14. M. Zhao, Y.-S. Guo, W.-N. Xu, Y.-F. Zhao, H.-Y. Xie, H.-J. Li, X.-F. Chen, R.-S. Zhao, D.-S. Guo, Far-red to near-infrared fluorescent probes based on silicon-substituted xanthene dyes for sensing and imaging. *TrAC, Trends Anal. Chem.* **122**, 115704 (2020).
15. F. Stuker, J. Ripoll, M. Rudin, Fluorescence molecular tomography: principles and potential for pharmaceutical research. *Pharmaceutics* **3**, 229-274 (2011).
16. X. Hadoux, F. Hui, J. K. H. Lim, C. L. Masters, A. Pébay, S. Chevalier, J. Ha, S. Loi, C. J. Fowler, C. Rowe, V. L. Villemagne, E. N. Taylor, C. Fluke, J.-P. Soucy, F. Lesage, J.-P. Sylvestre, P. Rosa-Neto, S. Mathotaarachchi, S. Gauthier, Z. S. Nasreddine, J. D. Arbour, M.-A. Rhéaume, S. Beaulieu, M. Dirani, C. T. O. Nguyen, B. V. Bui, R. Williamson, J. G. Crowston, P. van Wijngaarden, Non-invasive in vivo

hyperspectral imaging of the retina for potential biomarker use in Alzheimer's disease. *Nat. Commun.* **10**, 4227 (2019).

17. H. Rai, S. Gupta, S. Kumar, J. Yang, S. K. Singh, C. Ran, G. Modi, Near-Infrared Fluorescent Probes as Imaging and Theranostic Modalities for Amyloid-Beta and Tau Aggregates in Alzheimer's Disease. *J. Med. Chem.* **65**, 8550-8595 (2022).
18. B. C. Uzuegbunam, D. Librizzi, B. Hooshyar Yousefi, PET Radiopharmaceuticals for Alzheimer's Disease and Parkinson's Disease Diagnosis, the Current and Future Landscape. *Molecules* **25**, 977 (2020).
19. H. Watanabe, M. Ono, K. Matsumura, M. Yoshimura, H. Kimura, H. Saji, Molecular imaging of β-amyloid plaques with near-infrared boron dipyrromethane (BODIPY)-based fluorescent probes. *Mol. Imaging* **12**, 338-347 (2013).
20. C. L. Teoh, D. Su, S. Sahu, S. W. Yun, E. Drummond, F. Prelli, S. Lim, S. Cho, S. Ham, T. Wisniewski, Y. T. Chang, Chemical Fluorescent Probe for Detection of Aβ Oligomers. *J. Am. Chem. Soc.* **137**, 13503-13509 (2015).
21. H. Yang, F. Zeng, Y. Luo, C. Zheng, C. Ran, J. Yang, Curcumin Scaffold as a Multifunctional Tool for Alzheimer's Disease Research. *Molecules* **27**, (2022).
22. H. Fu, P. Tu, L. Zhao, J. Dai, B. Liu, M. Cui, Amyloid-β Deposits Target Efficient Near-Infrared Fluorescent Probes: Synthesis, in Vitro Evaluation, and in Vivo Imaging. *Anal. Chem.* **88**, 1944-1950 (2016).
23. Y. Jung, J. Jung, Y. Huh, D. Kim, Benzo[g]coumarin-Based Fluorescent Probes for Bioimaging Applications. *J. Anal. Methods Chem.* **2018**, 5249765 (2018).
24. G. Lv, Y. Shen, W. Zheng, J. Yang, C. Li, J. Lin, Fluorescence Detection and Dissociation of Amyloid-β Species for the Treatment of Alzheimer's Disease. *Adv. Ther.* **2**, 1900054 (2019).
25. C. Ran, X. Xu, S. B. Raymond, B. J. Ferrara, K. Neal, B. J. Bacskai, Z. Medarova, A. Moore, Design, Synthesis, and Testing of Difluoroboron-Derivatized Curcumins as Near-Infrared Probes for in Vivo Detection of Amyloid-β Deposits. *J. Am. Chem. Soc.* **131**, 15257-15261 (2009).
26. Y. Li, K. Wang, K. Zhou, W. Guo, B. Dai, Y. Liang, J. Dai, M. Cui, Novel D–A–D based near-infrared probes for the detection of β-amyloid and Tau fibrils in Alzheimer's disease. *Chem. Comm.* **54**, 8717-8720 (2018).
27. L. Cai, R. B. Innis, V. W. Pike, Radioligand development for PET imaging of beta-amyloid (Abeta)--current status. *Curr. Med. Chem.* **14**, 19-52 (2007).
28. N. H. Kim, Y. Huh, D. Kim, Benzo[g]coumarin-benzothiazole hybrid: A fluorescent probe for the detection of amyloid-beta aggregates. *Bull. Korean Chem. Soc.* **43**, 764-768 (2022).
29. J. Shin, P. Verwilst, H. Choi, S. Kang, J. Han, N. H. Kim, J. G. Choi, M. S. Oh, J. S. Hwang, D. Kim, I. Mook-Jung, J. S. Kim, Harnessing Intramolecular Rotation To Enhance Two-photon Imaging of Aβ Plaques through Minimizing Background Fluorescence. *Angew. Chem. Int. Ed.* **58**, 5648-5652 (2019).
30. K. Rajasekhar, N. Narayanaswamy, N. A. Murugan, K. Viccaro, H. G. Lee, K. Shah, T. Govindaraju, Aβ plaque-selective NIR fluorescence probe to differentiate Alzheimer's disease from tauopathies.

Biosens. Bioelectron. **98**, 54-61 (2017).

31. A. A. Elbatrawy, S. J. Hyeon, N. Yue, E. E. A. Osman, S. H. Choi, S. Lim, Y. K. Kim, H. Ryu, M. Cui, G. Nam, “Turn-On” Quinoline-Based Fluorescent Probe for Selective Imaging of Tau Aggregates in Alzheimer’s Disease: Rational Design, Synthesis, and Molecular Docking. *ACS Sens.* **6**, 2281-2289 (2021).
32. B. Zhu, T. Zhang, Q. Jiang, Y. Li, Y. Fu, J. Dai, G. Li, Q. Qi, Y. Cheng, Synthesis and evaluation of pyrazine and quinoxaline fluorophores for in vivo detection of cerebral tau tangles in Alzheimer's models. *Chem. Comm.* **54**, 11558-11561 (2018).
33. K. Zhou, C. Yuan, B. Dai, K. Wang, Y. Chen, D. Ma, J. Dai, Y. Liang, H. Tan, M. Cui, Environment-Sensitive Near-Infrared Probe for Fluorescent Discrimination of Aβ and Tau Fibrils in AD Brain. *J. Med. Chem.* **62**, 6694-6704 (2019).
34. L. Gu, Z. Guo, Alzheimer's Aβ42 and Aβ40 peptides form interlaced amyloid fibrils. *J. Neurochem.* **126**, 305-311 (2013).
35. G.-f. Chen, T.-h. Xu, Y. Yan, Y.-r. Zhou, Y. Jiang, K. Melcher, H. E. Xu, Amyloid beta: structure, biology and structure-based therapeutic development. *Acta Pharmacol. Sin.* **38**, 1205-1235 (2017).
36. I. A. Mastrangelo, M. Ahmed, T. Sato, W. Liu, C. Wang, P. Hough, S. O. Smith, High-resolution atomic force microscopy of soluble Abeta42 oligomers. *J. Mol. Biol.* **358**, 106-119 (2006).
37. W. E. Klunk, Y. Wang, G. F. Huang, M. L. Debnath, D. P. Holt, C. A. Mathis, Uncharged thioflavin-T derivatives bind to amyloid-beta protein with high affinity and readily enter the brain. *Life Sci.* **69**, 1471-1484 (2001).
38. J. Wang, H. Tanila, J. Puoliväli, I. Kadish, T. van Groen, Gender differences in the amount and deposition of amyloidbeta in APPswe and PS1 double transgenic mice. *Neurobiol. Dis.* **14**, 318-327 (2003).
39. M. Koronyo-Hamaoui, Y. Koronyo, A. V. Ljubimov, C. A. Miller, M. K. Ko, K. L. Black, M. Schwartz, D. L. Farkas, Identification of amyloid plaques in retinas from Alzheimer's patients and noninvasive in vivo optical imaging of retinal plaques in a mouse model. *Neuroimage* **54 Suppl 1**, S204-217 (2011).
40. M. Marquié, S. Valero, M. Castilla-Marti, J. Martínez, O. Rodríguez-Gómez, Á. Sanabria, J. P. Tartari, G. C. Monté-Rubio, O. Sotolongo-Grau, M. Alegret, A. Pérez-Cordón, N. Roberto, I. de Rojas, S. Moreno-Grau, L. Montrreal, I. Hernández, M. Rosende-Roca, A. Mauleón, L. Vargas, C. Abdelnour, S. Gil, E. Esteban-De Antonio, A. Espinosa, G. Ortega, F. Lomeña, J. Pavia, A. Vivas, M. Á. Tejero, M. Gómez-Chiari, R. Simó, A. Ciudin, C. Hernández, A. Orellana, A. Benaque, A. Ruiz, L. Tárraga, M. Boada, N. Aguilera, M. Berthier, M. Buendia, S. Bullich, F. Campos, P. Cañabate, C. Cuevas, A. Gailhajanet, J. Giménez, R. Gismondi, M. Guitart, M. Ibarria, A. Lafuente, E. Martín, M. Moreno, A. B. Nogales, L. Núñez, A. Páez, A. Pancho, E. Pelejà, V. Pérez-Grijalba, P. Pesini, S. Preckler, J. Romero, S. Ruiz, M. Sarasa, M. Torres, F. s. g. on behalf of the, Association between retinal thickness and β-amyloid brain accumulation in individuals with subjective cognitive decline: Fundació ACE Healthy Brain Initiative. *Alzheimers Res. Ther.* **12**, 37 (2020).

41. J. Yang, J. Yang, Y. Li, Y. Xu, C. Ran, Near-infrared Fluorescence Ocular Imaging (NIRFOI) of Alzheimer's Disease. *Mol. Imaging Biol.* **21**, 35-43 (2019).
42. A. Finelli, A. Kelkar, H. J. Song, H. Yang, M. Konsolaki, A model for studying Alzheimer's Abeta42-induced toxicity in Drosophila melanogaster. *Mol. Cell Neurosci.* **26**, 365-375 (2004).
43. Y. Yang, D. Arseni, W. Zhang, M. Huang, S. Lovestam, M. Schweighauser, A. Kotecha, A. G. Murzin, S. Y. Peak-Chew, J. Macdonald, I. Lavenir, H. J. Garringer, E. Gelpi, K. L. Newell, G. G. Kovacs, R. Vidal, B. Ghetti, B. Ryskeldi-Falcon, S. H. W. Scheres, M. Goedert, Cryo-EM structures of amyloid-beta 42 filaments from human brains. *Science* **375**, 167-172 (2022).
44. J. Yang, B. Zhu, W. Yin, Z. Han, C. Zheng, P. Wang, C. Ran, Differentiating Abeta40 and Abeta42 in amyloid plaques with a small molecule fluorescence probe. *Chem. Sci.* **11**, 5238-5245 (2020).
45. S. Maeda, N. Sahara, Y. Saito, M. Murayama, Y. Yoshiike, H. Kim, T. Miyasaka, S. Murayama, A. Ikai, A. Takashima, Granular tau oligomers as intermediates of tau filaments. *Biochem.* **46**, 3856-3861 (2007).
46. D. R. Beriault, G. H. Werstuck, Detection and quantification of endoplasmic reticulum stress in living cells using the fluorescent compound, Thioflavin T. *Biochim. Biophys. Acta Mol. Cell Res. BBA-MOL. CELL RES.* **1833**, 2293-2301 (2013).
47. M. J. Frisch, G. W. Trucks, H. B. Schlegel, G. E. Scuseria, M. A. Robb, J. R. Cheeseman, G. Scalmani, V. Barone, G. A. Petersson, H. Nakatsuji, X. Li, M. Caricato, A. V. Marenich, J. Bloino, B. G. Janesko, R. Gomperts, B. Mennucci, H. P. Hratchian, J. V. Ortiz, A. F. Izmaylov, J. L. Sonnenberg, Williams, F. Ding, F. Lipparini, F. Egidi, J. Goings, B. Peng, A. Petrone, T. Henderson, D. Ranasinghe, V. G. Zakrzewski, J. Gao, N. Rega, G. Zheng, W. Liang, M. Hada, M. Ehara, K. Toyota, R. Fukuda, J. Hasegawa, M. Ishida, T. Nakajima, Y. Honda, O. Kitao, H. Nakai, T. Vreven, K. Throssell, J. A. Montgomery Jr., J. E. Peralta, F. Ogliaro, M. J. Bearpark, J. J. Heyd, E. N. Brothers, K. N. Kudin, V. N. Staroverov, T. A. Keith, R. Kobayashi, J. Normand, K. Raghavachari, A. P. Rendell, J. C. Burant, S. S. Iyengar, J. Tomasi, M. Cossi, J. M. Millam, M. Klene, C. Adamo, R. Cammi, J. W. Ochterski, R. L. Martin, K. Morokuma, O. Farkas, J. B. Foresman, D. J. Fox. (Wallingford, CT, 2016).
48. R. Dennington, T. A. Keith, J. M. J. S. I. S. M. Millam, KS, USA, GaussView 6.0. 16. (2016).
49. P. A. Ravindranath, S. Forli, D. S. Goodsell, A. J. Olson, M. F. Sanner, AutoDockFR: Advances in Protein-Ligand Docking with Explicitly Specified Binding Site Flexibility. *PLoS Comput. Biol.* **11**, e1004586 (2015).
50. O. Trott, A. J. Olson, AutoDock Vina: improving the speed and accuracy of docking with a new scoring function, efficient optimization, and multithreading. *J. Comput. Chem.* **31**, 455-461 (2010).
51. S. J. S. LigPrep, LLC, New York, NY, LigPrep. **2021**, (2021).
52. J. Eberhardt, D. Santos-Martins, A. F. Tillack, S. Forli, AutoDock Vina 1.2.0: New Docking Methods, Expanded Force Field, and Python Bindings. *J. Chem. Inf. Model.* **61**, 3891-3898 (2021).
53. R. A. Laskowski, M. B. Swindells, LigPlot+: Multiple Ligand–Protein Interaction Diagrams for Drug Discovery. *J. Chem. Inf. Model.* **51**, 2778-2786 (2011).

Schemes

Schemes 1 to 4 are available in the Supplementary Files section

Unnumbered Images

Unnumbered images from the manuscript are available in the Supplementary Files section.

Figures

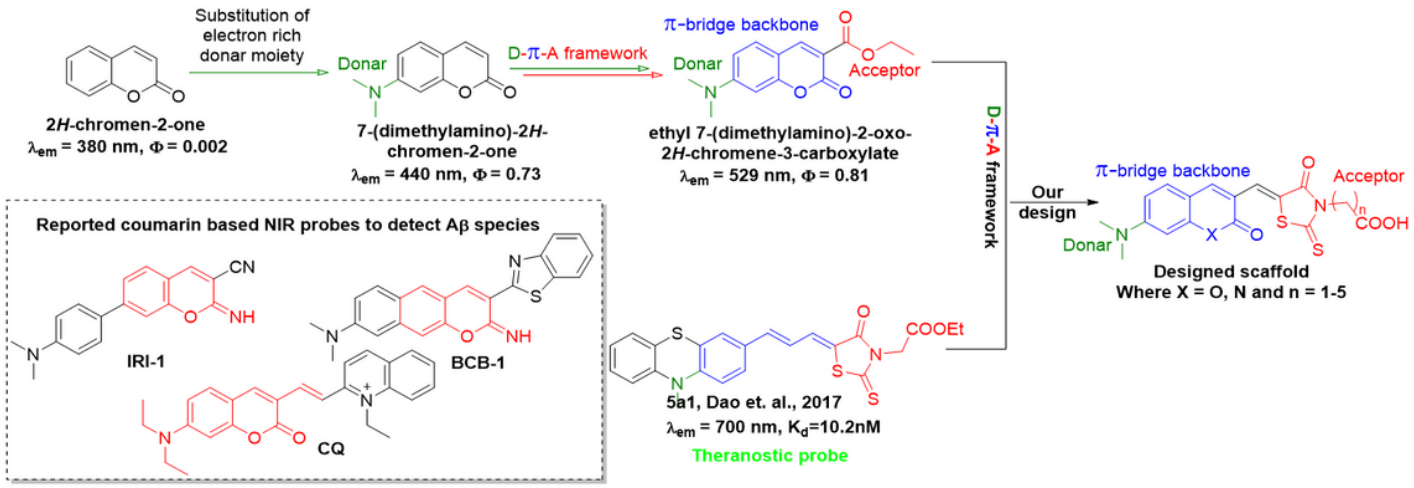

Figure 1

The rationale behind scaffold design. Change in the photophysical properties of coumarin with the aid of D-π-A architecture. Use of rhodanine acceptor fragment to achieve NIR range and improved target selectivity.

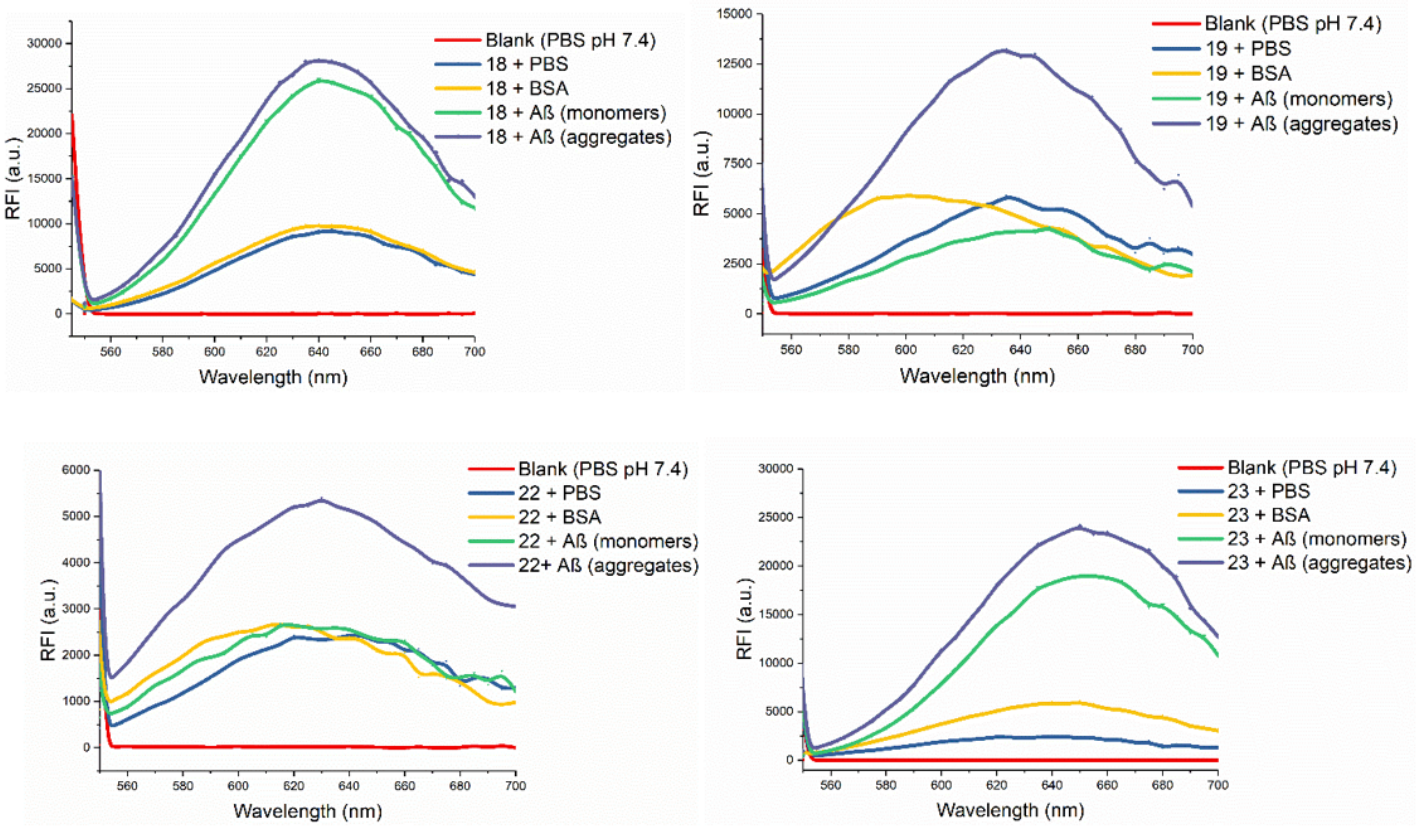

Figure 2

***In-vitro* fluorescence assay against Aβs and BSA.** The change in the fluorescence intensity of the tested probes (**18, 19, 22,** and **23**) upon incubation with various Aβs [monomers and aggregates] and BSA. The fluorescence spectra of the probes in PBS and PBS alone were also measured in the same condition.

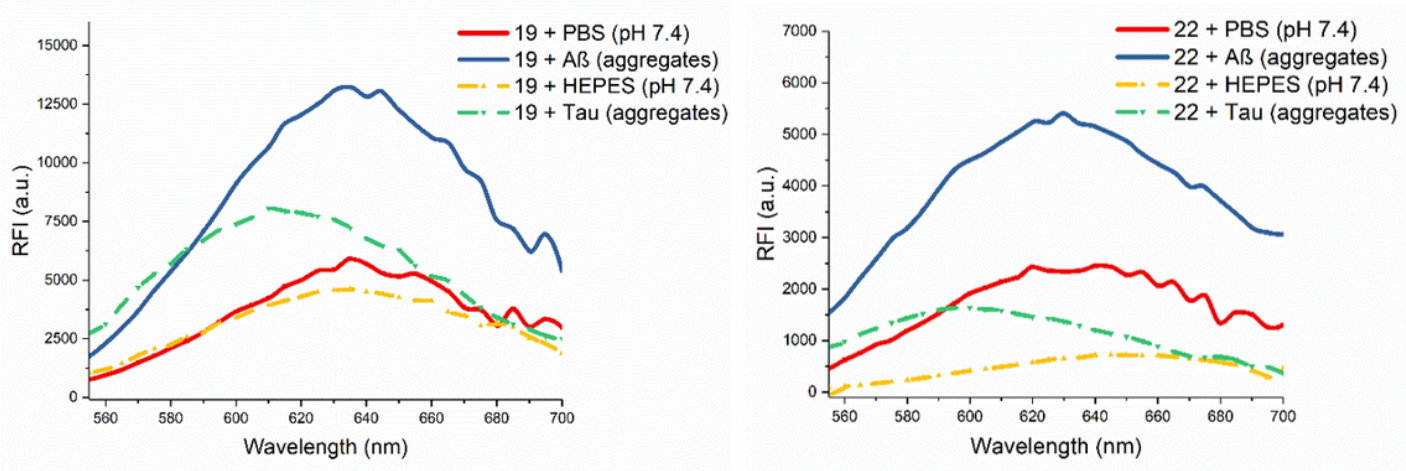

Figure 3

The fluorescence spectra of **19** and **22** at 20 μM concentration upon incubation with Tau aggregates (10 μM) and at 50 μM concentration upon incubation with Aβ aggregates (25 μM). Both the probes were prepared using 10x PBS and 10 mM Tris-HEPES assembly buffer (pH 7.4) with DMSO (2%) as a cosolvent in the *in-vitro* fluorescence assay.

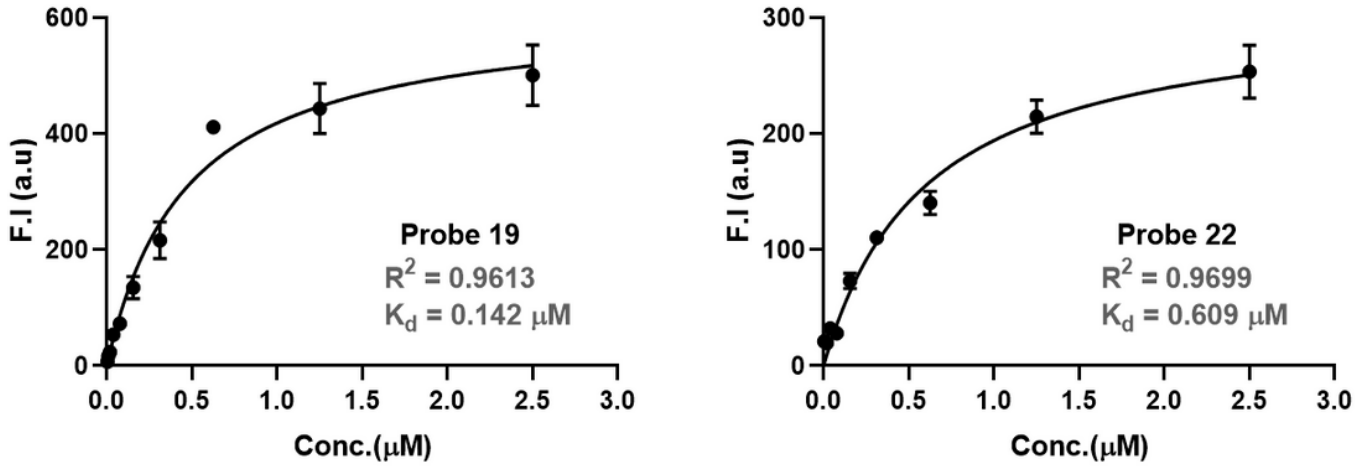

Figure 4

Saturation binding spectra against $A\beta_{1-42}$ aggregates. The saturation binding curve obtained on incubation of **19** and **22** at a gradient concentration range of 2.5-0.0075 μM upon incubation with 5.0 μM of $A\beta_{1-42}$ aggregates.

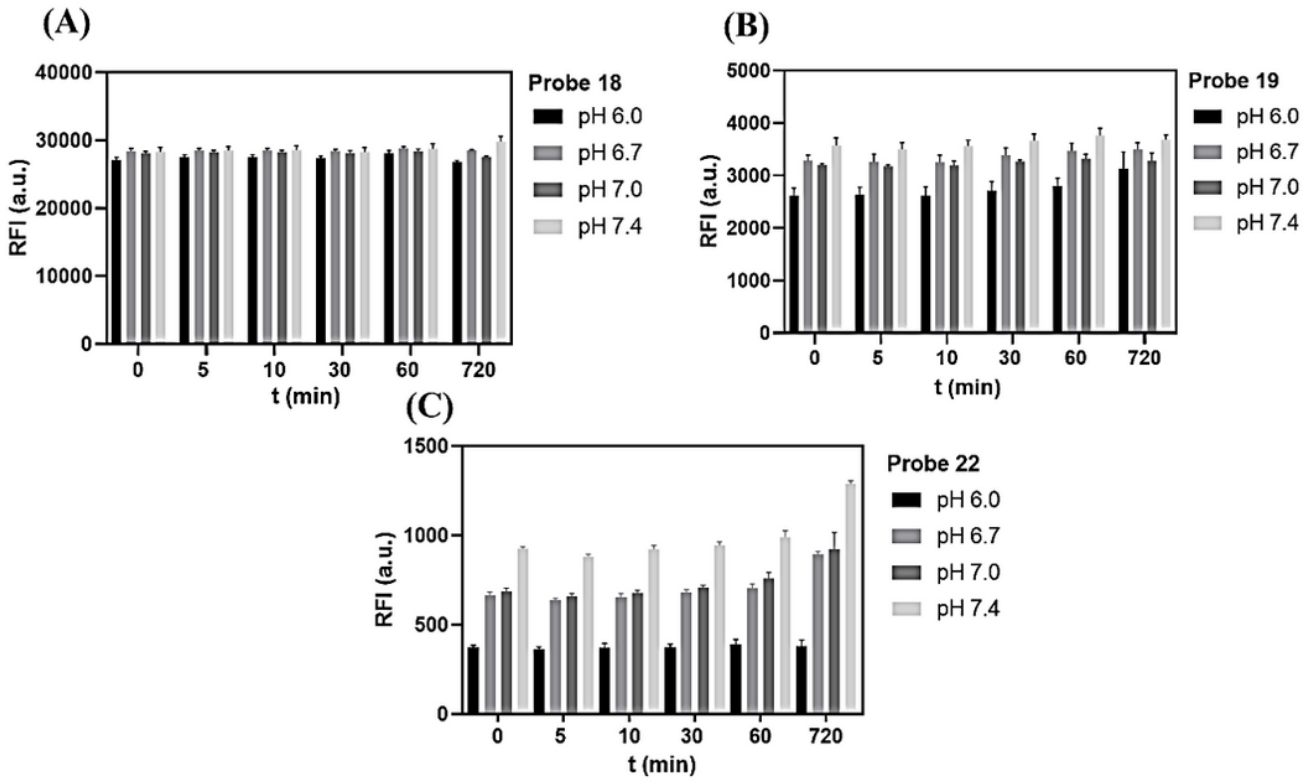

Figure 5

pH-dependent stability assay. Representative images are the bar diagram showing the relative fluorescence intensity (RFI) of probes **18 (A)**, **19 (B),** and **22 (C)** at various physiological pH recorded at 0-, 5-, 10-, 30-, 60, and 720 min. The pH range was 6.0, 6.7, 7.0, and 7.4, respectively, shown in the graph with different black and gray shades.

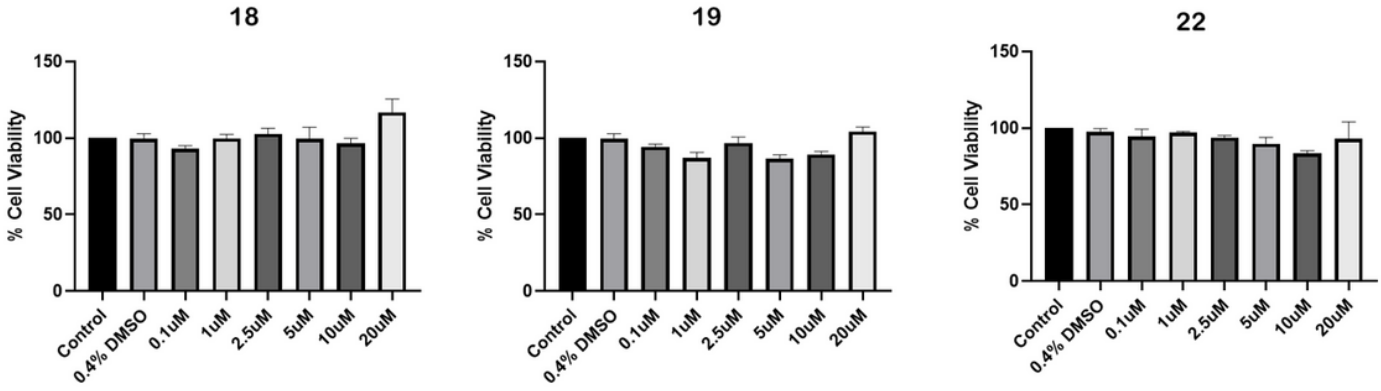

Figure 6

MTT assay of selective probes. Assessment of cytotoxicity of **18**, **19**, and **22** in the PC-12 cell line. Cells were treated with different concentrations of probes.

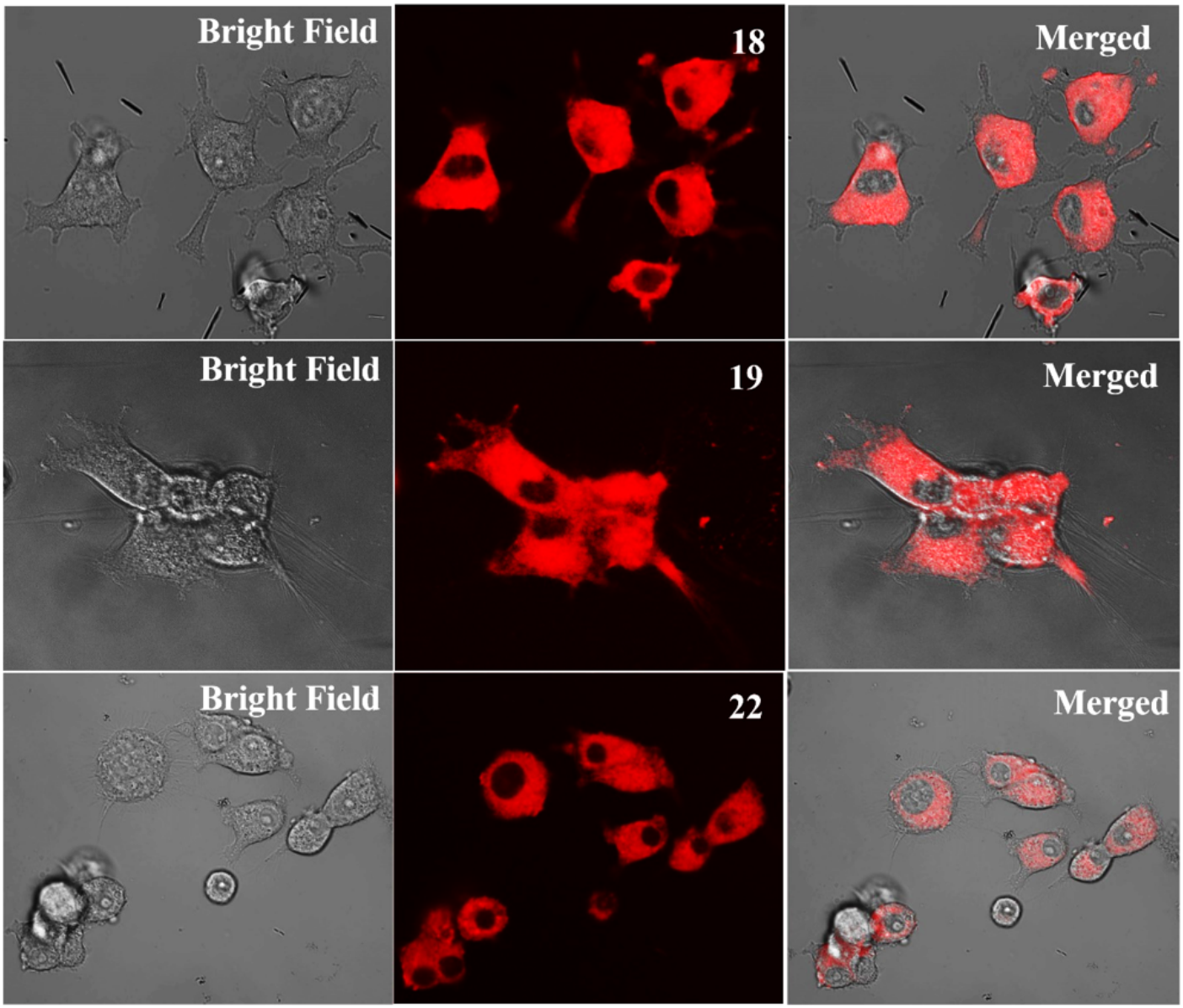

Figure 7

***In-vitro* cell internalization fluorescence assay.** Fluorescence microscope images visualizing **18**, **19**, and **22**internalizations at 10 μM in PC12 cells.

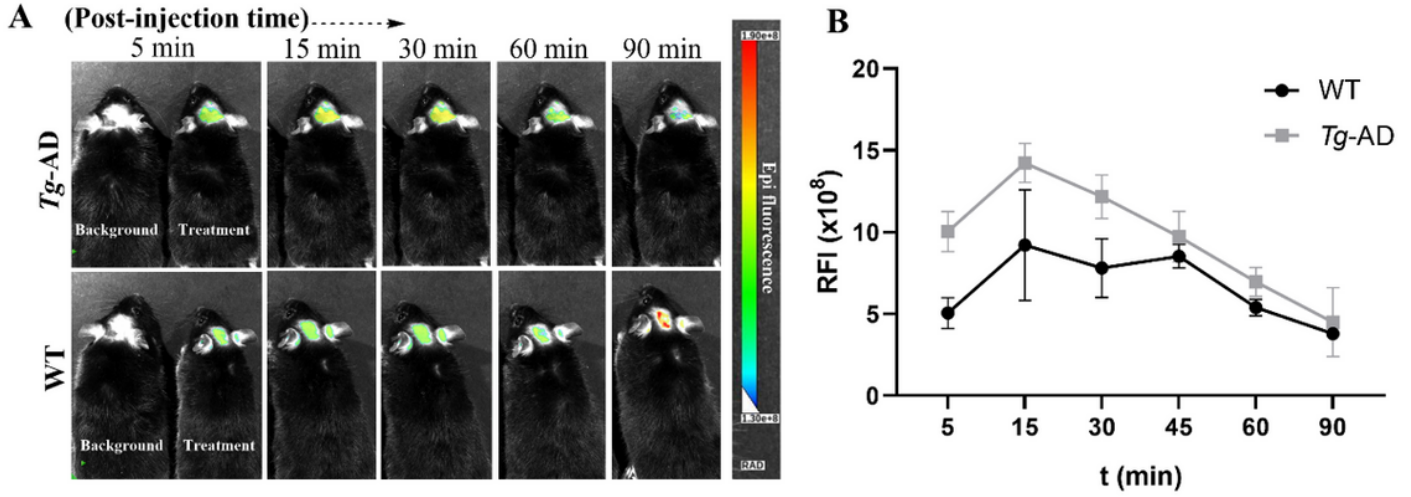

Figure 9

A: *In-vivo* NIR brain imaging in living mice. Representative brain images from *Tg*-AD (top row; n = 3 male mice) and WT (bottom row; n = 2 male) mice at representative post-injection time points of 0.8 mg/kg probe **19**. (λ_{ex} = 500 nm; λ_{em} = 630 nm; live fluorescence imaging was done using Lago-X from Spectral Instruments Imaging, equipped with desirable filter sets). **B**: Semi-quantitative analysis graph showing changes in brain signals (ROI) *vs* time (min) scale plot. The signal of WT mice's brains is relatively poor compared to the brain of *Tg*-AD mice.

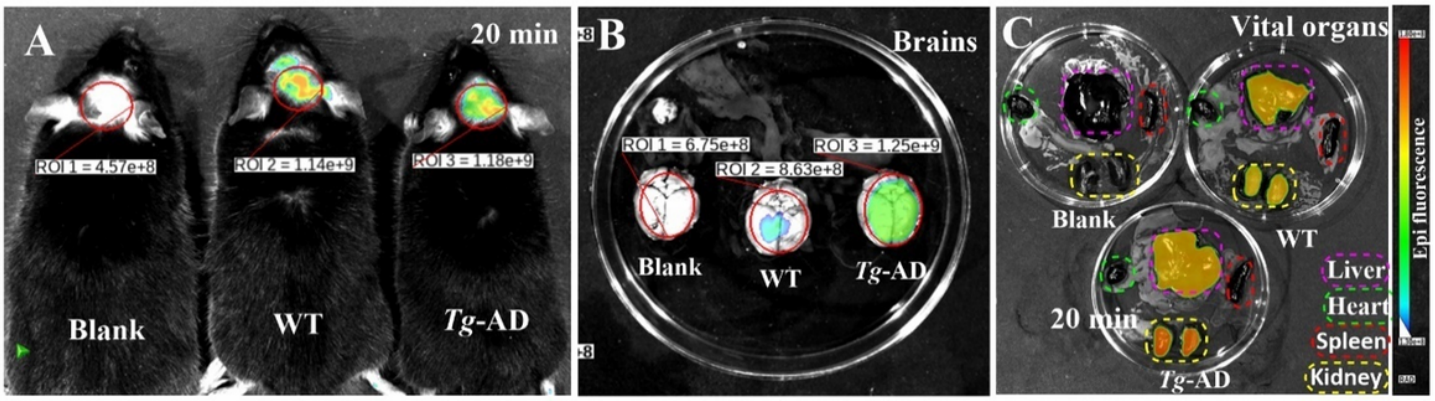

Figure 10

A: *Ex-vivo* fluorescence imaging and bio-distribution analysis of probe 19. Fluorescence NIR images of living mice at 20 min post intravenously injected probe **19** (0.8 mg/kg, the vehicle used for dilution consisting of 15 % of DMSO, 5% of Cremophor® EL, and 80% of 1X PBS) in *Tg*-AD and wild type (WT) mice. **B:** Fluorescence images of excised and perfused brains from blank (dosed with vehicle media only; control group), WT, and *Tg*-AD mice (treatment groups) sacrificed at 20 min after tail vein injection of probe **19**. **C:** Representative image of vital organs (liver, heart, spleen, and kidney) acquired from the same

mice used for ex-vivo fluorescence imaging of the whole intact brain (B). (λ_{ex} = 500 nm; λ_{em} = 630 nm; *in-vivo* and *ex vivo* imaging was done using a Lago-X spectral imaging instrument).

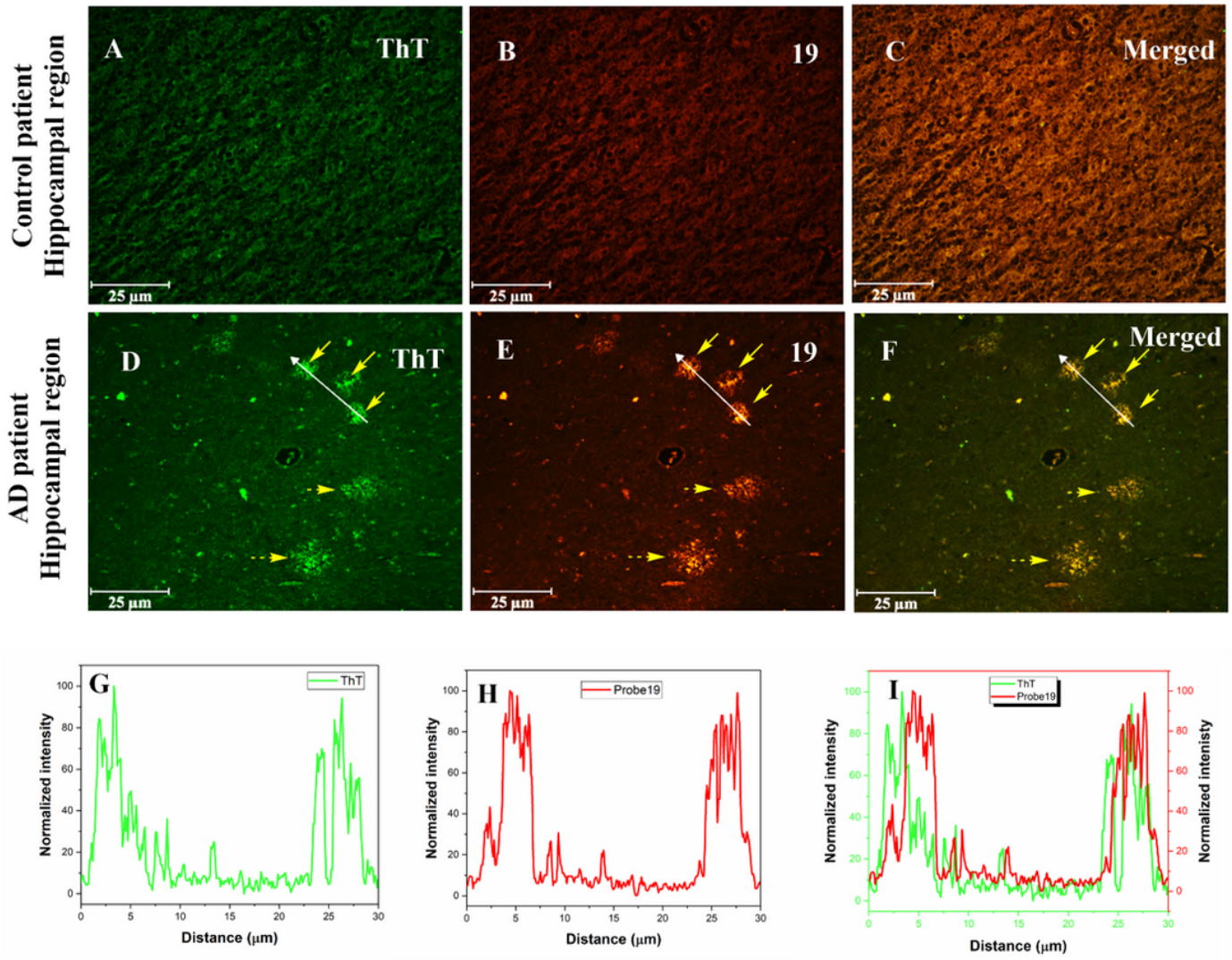

Figure 12

Confocal fluorescence images from in vitro staining of hippocampal brain autopsy sections from the 92-year-old control (row 1; female) and AD patient (row 2; female). ThT staining was used to confirm Aβs (A, D) using the FITC emission (green) filter. To validate selectivity for Aβ aggregates, the same slides were counterstained with probe **19,** and pictures were taken at the TRITC emission (red) filter (B, E). Yellow arrows represented cored plaques (with solid line) and diffuse plaques (dotted line). Merged images of corresponding slides show that ThT and probe **19** are colocalized (yellow stain). (Scale bar 25 µm; NIS-Elements BR 4.30.00.64-bit fluorescence microscope). **(G-I)** The signal intensity profile of ThT (G, Green line), probe **19** (H, red line) and merged (I, superposed green and red signals) in the linear ROI across white arrow line in D, E, and F.

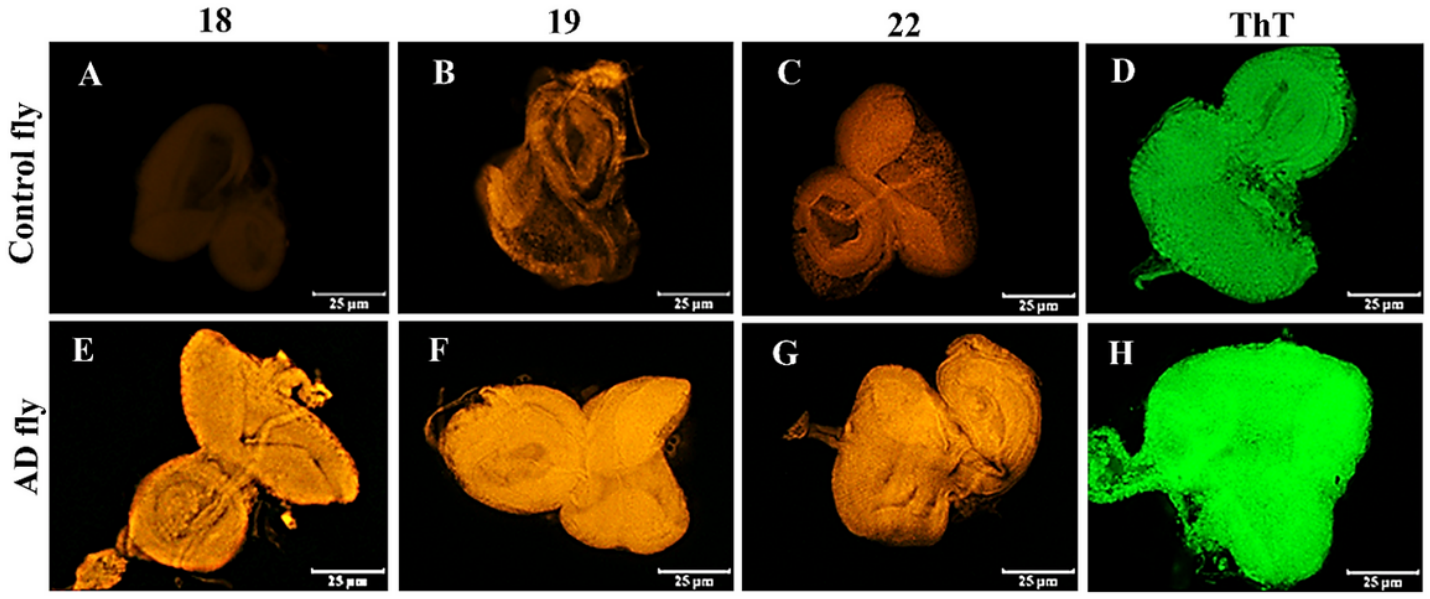

Figure 14

***Ex vivo* fluorescence microscope images of imaginal eye discs from L3 larvae**. The slides (A, E), (B, F), and (C, G) were stained with **18**, **19**, and **22**, respectively, and recorded using the TRITC filter set, while D and H were ThT-stained slides recorded using FITC filter set. Histologically stained ocular imaginal discs from control and age-matched AD larvae are shown in rows 1 and 2, respectively. (Scale bar: 25 µm, NIS-Elements BR 4.30.00.64-bit fluorescence microscope)

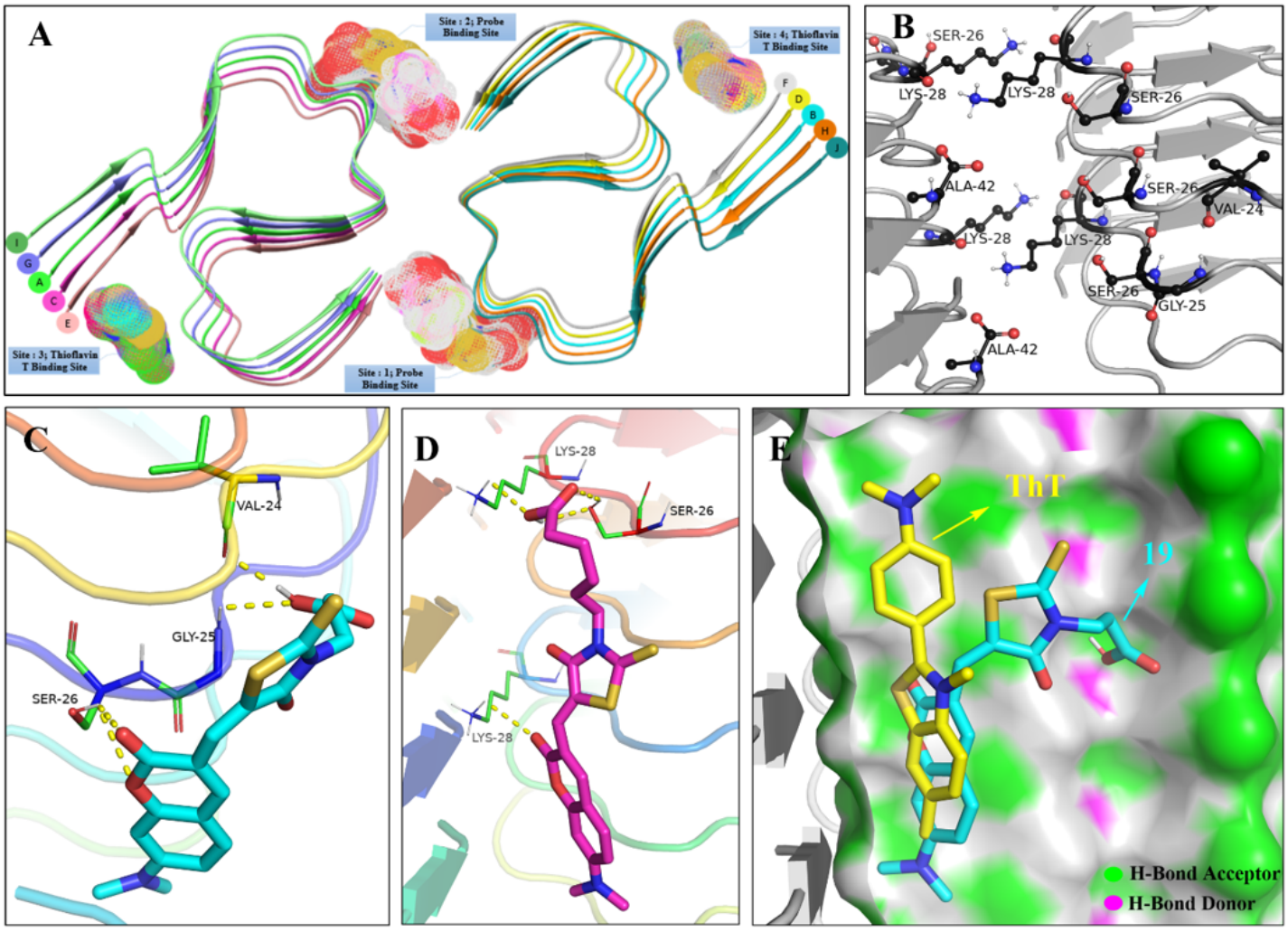

Figure 16

Mapping of binding sites based on average docking scores, amino acid residues within the binding pocket, and representative interaction diagrams. A: Aβ fibril (7Q4M) and four binding sites. **B:**Close-up view of probe binding pocket with interacting residues (Ball and Stick Model). **C** and **D:** 3D interactions of probe **19 (**cyan, stick mode**)** and **22 (**magenta, stick mode**)** with amino acid residues within the site-2 binding pocket; hydrogen bond interactions are represented by the yellow dotted line. **E:** Superimposed **ThT (**yellow, stick mode**)** and probe **19** within the binding pocket.

Supplementary Files

This is a list of supplementary files associated with this preprint. Click to download.

- SupplementaryInformation.docx
- floatimage1.png
- UnnumberedImages.docx

- Scheme1.png
- Scheme2.png
- Scheme3.png
- Scheme4.png